Research Square

Preprints are preliminary reports that have not undergone peer review.
They should not be considered conclusive, used to inform clinical practice,
or referenced by the media as validated information.

Comprehensive Modeling and Physical Analysis of Proposed FCC-ee Superconducting Solenoid System

Ethan Fajardo

ethan.fajardo@stonybrook.edu

Brookhaven National Laboratory

Vikas Teotia

Brookhaven National Laboratory

Research Article

Keywords: FCC-ee, superconducting detector magnets, inverse magnet design, fringe-field suppression, electromagnetic force analysis, OPERA-3D

Posted Date: November 17th, 2026

DOI: https://doi.org/10.21203/rs.3.rs-11705439/v1

License: This work is licensed under a Creative Commons Attribution 4.0 International License.
Read Full License

Additional Declarations: The authors declare no competing interests.

Comprehensive Modeling and Physical Analysis of Proposed FCC-ee Superconducting Solenoid System

Ethan Fajardo[1], Vikas Teotia[1]
[1]*Superconducting Magnet Division, Brookhaven National Laboratory, Upton, NY 11973, USA*

November 11, 2026

The Future Circular Collider electron–positron collider (FCC-ee), planned at CERN, requires an integrated detector-magnet system that produces a strong, well-controlled central field while suppressing fringe fields and limiting electromagnetic loads. Superconducting Magnet Division is designing magnets for the interaction region of FCC-ee including the main focusing quadrupole, correctors and compensations solenoids. This project focuses on the screening solenoid which annuls magnetic field generated by the detector solenoids at locations of the final focus quadruples. A primary detector solenoid and mirror-symmetric segmented screening coils are modeled using analytical finite-thickness solenoid fields. Differential Evolution optimizes the screening geometry, while bounded weighted least squares determine current densities that preserve the central field and suppress the axial field. The optimized configuration is exported to OPERA-3D for finite-element validation. The force methodology is first established using two identical coaxial solenoids, with analytical predictions compared against OPERA calculations over multiple separations to verify force direction, scaling, symmetry, and action–reaction balance. It is then applied to a more advanced optimized FCC-ee magnet model representing the logical next step of the inverse-design process. Forces on the main and screening coils are evaluated through conductor-level load distributions, mirror-pair residuals, and global force balance. An independent reconstruction is compared with full nonlinear and matched nonmagnetic OPERA models, validating the coil-only calculation and isolating the contribution of the iron yoke and calorimeter. The resulting workflow unifies inverse magnetic design, numerical force validation, and electromagnetic loading analysis for an optimized FCC-ee screening solenoid system. It supports Brookhaven and U.S. Department of Energy accelerator-magnet objectives while developing professional expertise in superconducting magnet design, optimization, finite-element analysis, and practical engineering interpretation skills.

Keywords: FCC-ee; superconducting detector magnets; inverse magnet design; fringe-field suppression; electromagnetic force analysis; OPERA-3D

1 Introduction

The proposed Future Circular Collider electron–positron collider (FCC-ee) is intended to support high-precision measurements of electroweak, Higgs-boson, and top-quark physics [1, 2]. Achieving this precision requires a detector solenoid capable of producing a strong, well-controlled magnetic field for charged-particle tracking while remaining compatible with the accelerator and detector systems surrounding the interaction region [1, 3, 4, 5].

A finite detector solenoid inevitably produces an extended fringe field outside its central tracking volume [3, 4, 6, 7]. These stray fields can interfere with nearby accelerator magnets, detector components, and magnetic return structures [1, 5, 8]. Screening solenoids provide a means of suppressing the external field while preserving the useful central field [3, 4, 5, 8], but their design introduces competing electromagnetic and engineering requirements. The screening geometry and current distribution must reproduce the desired field profile within geometric and current-density constraints, despite the inability of finite windings to generate an abrupt field cutoff [6, 7, 9].

Field performance alone is not sufficient to determine whether a screening system is physically viable [3, 4]. Interactions among the main solenoid, the screening conductors, and nearby magnetic materials can produce large and spatially nonuniform forces [3, 4, 9, 10]. In a mirror-symmetric system, these internal loads may cancel in the global force sum even though individual conductors and their supports remain heavily loaded [4, 9]. The nonlinear response of the detector yoke and calorimeter can further redistribute the magnetic field and alter the conductor-force distribution [3, 4]. A satisfactory design must therefore suppress the fringe field without introducing loads that cannot be realistically supported [3, 4].

This work develops a computational workflow that connects magnetic inverse design with electromagnetic validation and conductor-level force analysis. A target axial field is prescribed, and a mirror-symmetric segmented screening system is optimized using an analytical finite-thickness solenoid model, Differential Evolution, and bounded weighted least squares [6, 7, 11, 12]. The optimized configuration is then transferred to OPERA-3D for independent field validation and evaluation of nonlinear material effects.

The force-analysis procedure is first verified using a reduced two-solenoid benchmark and is subsequently applied to the complete optimized magnet. An independent coil-only force reconstruction is used to validate the

nonmagnetic OPERA solution, while comparison with the nonlinear model isolates the additional loading introduced by the iron yoke and calorimeter. The resulting framework is intended to determine not only whether the proposed screening system provides the required field confinement, but also whether its internal electromagnetic loading is consistent with the development of a realistic and mechanically supportable FCC-ee detector magnet and broader magnetic system [1, 3, 4, 5]

2 Theoretical and Computational Framework

2.1 Magnetic Field Model

The objective of this work is to shape the axial magnetic field of a primary superconducting solenoid so that a strong central field is preserved while the external fringe field is rapidly suppressed. The desired field is represented by a Gaussian-like profile with a prescribed axial cutoff,

$$B_{\text{target}}(z) = \begin{cases} B_0 \exp\left(-\frac{(z-z_0)^2}{2\sigma^2}\right), & |z - z_0| \le w, \\ 0, & |z - z_0| > w, \end{cases} \tag{1}$$

where B_0 is the target peak field, z_0 is the field center, σ controls the width of the central profile, and w defines the half-width of the preserved region. The abrupt transition to zero is intentionally idealized. A finite solenoid cannot generate a field with strict compact support because its magnetic field remains continuous and extends beyond the physical ends of the winding [6, 9].

The total field is written as the linear superposition of the main-solenoid field and the fields generated by the screening segments,

$$B_{\text{total}}(z) = B_{\text{main}}(z) + \sum_{i=1}^{N_s} B_i\,(z), \tag{2}$$

where N_s is the number of screening segments. The screening coils are arranged as mirror-symmetric chains on the two sides of the central field. Their current direction is chosen primarily to oppose the fringe field of the main solenoid, thereby reducing the axial wings while leaving the central region largely unchanged.

Each coil is modeled as a finite-thickness axisymmetric current distribution. For a solenoid with inner radius R_i, outer radius R_o, axial boundaries z_1 and z_2, and uniform current density J, the on-axis magnetic field is

$$B(z) = \frac{\mu_0 J}{2}\,[F(R_o, z) - F(R_i, z)], \tag{3}$$

where

$$\begin{aligned} F(R, z) = (z - z_2)\text{asinh}\left(\frac{R}{z - z_2}\right) - (z - z_1)\text{asinh}\left(\frac{R}{z - z_1}\right) \\ -\sqrt{R^2 + (z - z_2)^2} + \sqrt{R^2 + (z - z_1)^2}. \end{aligned} \tag{4}$$

This analytical expression [7] is used for the main solenoid and every screening segment. It is convenient to write the field of a segment as

$$B_i(z) = J_i K_i(z), \tag{5}$$

where $K_i(z)$ contains only the geometry of the segment. Equation (5) makes explicit that the magnetic field is linear in current density. This linearity is central to the segment-current solution.

2.2 Inverse Optimization Formulation

For a given candidate geometry, the quality of the field reconstruction is determined from the residual

$$r(z) = B_{\text{total}}(z) - B_{\text{target}}(z). \tag{6}$$

A single global error measure is insufficient because the optimization must satisfy several physically distinct requirements. In the central region, the screening field must not significantly distort the useful detector field. Near the target cutoff, the field must transition rapidly without producing a large overshoot. Farther from the central region, the remaining fringe field and any low-amplitude oscillations must be suppressed.

The objective function is therefore written as a weighted sum over the axial grid,

$$F = \sum_{j=1}^{N_z} w\,(z_j)\left[B_{\text{total}}(z_j) - B_{\text{target}}(z_j)\right]^2 + F_{\text{penalty}}, \tag{7}$$

where $w(z_j)$ is a region-dependent weight and F_{penalty} contains additional penalties associated with incomplete field coverage, invalid geometry, or other undesirable configurations. Larger weights are assigned to the protected

central field, the transition near the hard edge, and the far-wing region so that the optimizer does not reduce the broad average error at the expense of a locally poor field.

For a fixed screening geometry, the total field can be written in matrix form as

$$\boldsymbol{B}_{\mathrm{total}} = \boldsymbol{B}_{\mathrm{main}} + \boldsymbol{K}\boldsymbol{J}, \tag{8}$$

where $\boldsymbol{K}$ contains the field kernels of all screening segments and $\boldsymbol{J}$ is the vector of segment current densities. Because the current densities enter linearly, their optimal values are obtained using bounded weighted linear least squares,

$$\boldsymbol{J}^{*} = \underset{\boldsymbol{J}}{\mathrm{argmin}} \left\| \boldsymbol{W}^{1/2}\left(\boldsymbol{B}_{\mathrm{main}} + \boldsymbol{K}\boldsymbol{J} - \boldsymbol{B}_{\mathrm{target}}\right) \right\|_2^2, \tag{9}$$

subject to

$$J_{i,\mathrm{min}} \le J_i \le J_{i,\mathrm{max}}. \tag{10}$$

The sign convention is chosen such that the primary screening segments generate a field opposing the main-solenoid wings. Optional trim segments may be permitted to take either sign so that small oscillatory residuals can be corrected after the primary cancellation has been established.

Differential Evolution is then used to optimize the nonlinear geometric parameters of the screening chain [11, 12]. These variables may include the common inner radius and radial thickness of the screening winding, the axial start position, the number of active segments, and the individual segment lengths. For every trial geometry, the segment kernels are constructed, the current densities are solved using Eq. (9), and the resulting field is evaluated using Eq. (7).

The full inverse-design problem may therefore be expressed as

$$\min_{\boldsymbol{g}} F[\boldsymbol{g}, \boldsymbol{J}^{*}(\boldsymbol{g})], \tag{11}$$

where $\boldsymbol{g}$ denotes the geometric design variables and $\boldsymbol{J}^{*}(\boldsymbol{g})$ is the bounded least-squares current solution for that geometry. This separation reduces the dimensionality of the global search because Differential Evolution does not need to search the current densities directly.

After an optimized configuration is obtained, the residual field is examined over the axial interval occupied by each segment and the screening chain is refined adaptively. The segment associated with the largest weighted residual is identified and subdivided, introducing an additional spatial degree of freedom where the field agreement is poorest, and the entire chain is then re-optimized. This process allows shorter segments to emerge near the sharp field transition and longer segments to remain in smoother far-wing regions.

2.3 Analytical Two-Solenoid Force Derivation

The analytical force model is developed in four steps. First, the magnetic field of a current distribution is obtained from the magnetostatic Maxwell equations. This result is then applied to a circular current loop and extended to a finite solenoid. The formulation is subsequently generalized to two coaxial solenoids through their self- and mutual inductances. Finally, a small-solenoid approximation is introduced to obtain a closed-form force expression and its large-separation limit.

For steady currents, Maxwell's equations reduce to

$$\nabla \cdot \boldsymbol{B} = 0, \tag{12}$$

and

$$\nabla \times \boldsymbol{B} = \mu_0 \boldsymbol{J}. \tag{13}$$

Because the magnetic field is divergence-free, it may be written in terms of a vector potential,

$$\boldsymbol{B} = \nabla \times \boldsymbol{A}. \tag{14}$$

Substituting Eq. (14) into Eq. (13) gives

$$\nabla \times (\nabla \times \boldsymbol{A}) = \mu_0 \boldsymbol{J}. \tag{15}$$

Using the vector identity

$$\nabla \times (\nabla \times \boldsymbol{A}) = \nabla(\nabla \cdot \boldsymbol{A}) - \nabla^2 \boldsymbol{A}, \tag{16}$$

and selecting the Coulomb gauge,

$$\nabla \cdot \boldsymbol{A} = 0, \tag{17}$$

the vector potential satisfies Poisson's equation,

$$\nabla^2 \boldsymbol{A} = -\mu_0 \boldsymbol{J}. \tag{18}$$

The corresponding free-space solution is

$$\boldsymbol{A}(\boldsymbol{r}) = \frac{\mu_0}{4\pi} \int \frac{\boldsymbol{J}(\boldsymbol{r}')}{|\boldsymbol{r}-\boldsymbol{r}'|} \, \mathrm{d}^3 r'. \tag{19}$$

Taking the curl of Eq. (19) produces the Biot–Savart law,

$$\boldsymbol{B}(\boldsymbol{r}) = \frac{\mu_0}{4\pi} \int \boldsymbol{J}(\boldsymbol{r}') \times \frac{\boldsymbol{r}-\boldsymbol{r}'}{|\boldsymbol{r}-\boldsymbol{r}'|^3} \, \mathrm{d}^3 r'. \tag{20}$$

For a thin wire carrying current I,

$$\boldsymbol{J}(\boldsymbol{r}') \, \mathrm{d}^3 r' = I \, \mathrm{d}\boldsymbol{\ell}', \tag{21}$$

so Eq. (20) becomes

$$\boldsymbol{B}(\boldsymbol{r}) = \frac{\mu_0 I}{4\pi} \oint \frac{\mathrm{d}\boldsymbol{\ell}' \times (\boldsymbol{r}-\boldsymbol{r}')}{|\boldsymbol{r}-\boldsymbol{r}'|^3}. \tag{22}$$

Equation (22) provides the starting point for the magnetic field of a circular loop.

Consider a circular loop of radius R, centered on the z-axis and carrying current I. At an axial distance s from the loop center, azimuthal symmetry causes all transverse magnetic-field components to cancel. Only the axial component remains,

$$B_{\mathrm{loop},z}(s) = \frac{\mu_0 I R^2}{2(R^2+s^2)^{3/2}}. \tag{23}$$

A finite thin-walled solenoid may be treated as a continuous axial distribution of such loops. For a solenoid with N turns and axial length L, the turn density is

$$n = \frac{N}{L}. \tag{24}$$

Let the solenoid be centered at $z = z_c$, with individual turns distributed over

$$-\frac{L}{2} \le z' \le \frac{L}{2}. \tag{25}$$

The contribution from an axial element $\mathrm{d}z'$ is obtained from Eq. (23) by using

$$\mathrm{d}N = n \, \mathrm{d}z'. \tag{26}$$

The total on-axis field is therefore

$$B_z(z) = \frac{\mu_0 n I R^2}{2} \int_{-L/2}^{L/2} \frac{\mathrm{d}z'}{[R^2+(z-z_c-z')^2]^{3/2}}. \tag{27}$$

Evaluating the integral gives

$$B_z(z) = \frac{\mu_0 N I}{2L} \left[\frac{z-z_c+L/2}{\sqrt{R^2+(z-z_c+L/2)^2}} - \frac{z-z_c-L/2}{\sqrt{R^2+(z-z_c-L/2)^2}} \right]. \tag{28}$$

The analytical model uses the mean winding radius,

$$R = \frac{r_{\mathrm{in}}+r_{\mathrm{out}}}{2}, \tag{29}$$

and represents the finite radial winding thickness through the equivalent ampere-turns

$$\mathcal{A} \equiv NI = J t_r L, \qquad t_r = r_{\mathrm{out}} - r_{\mathrm{in}}, \tag{30}$$

where J is the uniform engineering current density used in OPERA. The individual values of N and I therefore do not need to be specified separately.

Using $\mathcal{A} = NI$, the on-axis field becomes

$$B_z(z) = \frac{\mu_0 \mathcal{A}}{2L} \left[\frac{z-z_c+L/2}{\sqrt{R^2+(z-z_c+L/2)^2}} - \frac{z-z_c-L/2}{\sqrt{R^2+(z-z_c-L/2)^2}} \right]. \tag{31}$$

Now consider two coaxial solenoids with centers located at

$$z_1 = -\frac{D}{2}, \qquad z_2 = +\frac{D}{2}, \tag{32}$$

where

$$D = z_2 - z_1 \tag{33}$$

is their center-to-center separation. Each isolated winding has a self-inductance. For coil i, the self-inductance is defined by

$$L_i^{\mathrm{self}} = \frac{N_i \Phi_{ii}}{I_i}, \tag{34}$$

where Φ_{ii} is the magnetic flux through one turn of coil i generated by its own current.

When two coils are present, the field of one coil also links the turns of the other. Their mutual inductance is defined by

$$M(D) = \frac{N_2 \Phi_{21}}{I_1} = \frac{N_1 \Phi_{12}}{I_2}, \tag{35}$$

where Φ_{21} is the flux through coil 2 generated by coil 1. Unlike the self-inductances, the mutual inductance depends on the coil separation.

At fixed currents, the magnetic co-energy of the two-coil system is

$$W' = \frac{1}{2} L_1^{\mathrm{self}} I_1^2 + \frac{1}{2} L_2^{\mathrm{self}} I_2^2 + M(D) I_1 I_2. \tag{36}$$

The coils are assumed to remain rigid as D changes. Their lengths, radii, and winding distributions therefore remain fixed, so

$$\frac{\mathrm{d}L_1^{\mathrm{self}}}{\mathrm{d}D} = \frac{\mathrm{d}L_2^{\mathrm{self}}}{\mathrm{d}D} = 0. \tag{37}$$

The self-inductance terms describe stored energy and internal winding stress, but they do not produce a translational force between the two rigid coils. Only the mutual-inductance term changes with separation. The generalized force along the separation coordinate is therefore

$$F_D = \frac{\partial W'}{\partial D}\Big|_{I_1, I_2} = I_1 I_2 \frac{\mathrm{d}M}{\mathrm{d}D}. \tag{38}$$

Because the magnetic coupling decreases as the coils move apart,

$$\frac{\mathrm{d}M}{\mathrm{d}D} < 0. \tag{39}$$

Thus, currents flowing in the same direction produce $F_D < 0$, meaning that the force acts to reduce D and the coils attract. Reversing one current changes the sign of $I_1 I_2$ and makes the interaction repulsive.

A more complete thin-walled model can be constructed by integrating the mutual inductance of pairs of circular loops. For two coaxial circular current filaments of radii R_1 and R_2 separated axially by s, the mutual inductance is given by the Maxwell–Grover expression [10],

$$M_{\mathrm{loop}}(R_1, R_2, s) = \frac{\mu_0 \sqrt{R_1 R_2}}{k}\left[(2 - k^2)K(k) - 2E(k)\right], \tag{40}$$

where

$$k^2 = \frac{4 R_1 R_2}{(R_1 + R_2)^2 + s^2}, \tag{41}$$

and $K(k)$ and $E(k)$ are complete elliptic integrals of the first and second kind, respectively.

Using local axial coordinates ζ_1 and ζ_2, the separation between a loop in coil 1 and a loop in coil 2 is

$$s = D + \zeta_2 - \zeta_1. \tag{42}$$

The mutual inductance of the two finite thin-walled solenoids is then

$$M_{\mathrm{sol}}(D) = n_1 n_2 \int_{-L_1/2}^{L_1/2} \int_{-L_2/2}^{L_2/2} M_{\mathrm{loop}}\left(R_1, R_2, D + \zeta_2 - \zeta_1\right) \mathrm{d}\zeta_2 \, \mathrm{d}\zeta_1. \tag{43}$$

Together with Eq. (38), this provides a finite-length thin-sheet force model. However, evaluating it requires a two-dimensional numerical integration. A simpler closed-form expression is obtained by treating the receiving solenoid as a magnetic dipole.

Coil 1 is retained as a finite source solenoid, while coil 2 is replaced by a magnetic dipole located at its center. This approximation is appropriate when the magnetic field and its axial gradient generated by coil 1 vary only weakly across the dimensions of coil 2, which becomes increasingly valid as the separation grows relative to the coil radius and length. It therefore provides a simple reduced-order benchmark, with the greatest accuracy expected in the large-separation regime. The magnetic moment of coil 2 is

$$\boldsymbol{m}_2 = N_2 I_2 \pi R_2^2 \hat{\boldsymbol{z}} = \mathcal{A}_2 \pi R_2^2 \hat{\boldsymbol{z}}. \tag{44}$$

The force on a magnetic dipole in an external field is

$$\boldsymbol{F}_2 \simeq \nabla(\boldsymbol{m}_2 \cdot \boldsymbol{B}_1). \tag{45}$$

Because both the field and the magnetic moment are directed along the common axis,

$$F_{z,2} \simeq m_2 \left.\frac{\mathrm{d}B_{1,z}}{\mathrm{d}z}\right|_{z=z_2}. \tag{46}$$

This approximation requires the source field and its gradient to vary only weakly across the dimensions of coil 2. It is therefore most accurate when the receiving coil is small compared with its distance from the source coil. It is not expected to be exact when the two finite coils are closely spaced.

Differentiating the finite-solenoid field of coil 1 gives

$$\frac{\mathrm{d}B_{1,z}}{\mathrm{d}z} = \frac{\mu_0 \mathcal{A}_1 R_1^2}{2L_1}\left[\frac{1}{\left[R_1^2+(z-z_1+L_1/2)^2\right]^{3/2}} - \frac{1}{\left[R_1^2+(z-z_1-L_1/2)^2\right]^{3/2}}\right]. \tag{47}$$

At the center of coil 2,

$$z_2 - z_1 = D, \tag{48}$$

and the approximate force becomes

$$F_{z,2}^{\text{approx}}(D) = \frac{\mu_0 \pi \mathcal{A}_1 \mathcal{A}_2 R_1^2 R_2^2}{2L_1}\left[\frac{1}{\left[R_1^2+(D+L_1/2)^2\right]^{3/2}} - \frac{1}{\left[R_1^2+(D-L_1/2)^2\right]^{3/2}}\right]. \tag{49}$$

For identical solenoids,

$$R_1 = R_2 = R, \qquad L_1 = L_2 = L, \qquad \mathcal{A}_1 = \mathcal{A}_2 = \mathcal{A}, \tag{50}$$

so the force magnitude is

$$\boxed{\left|F_z^{\text{approx}}(D)\right| = \frac{\mu_0 \pi \mathcal{A}^2 R^4}{2L}\left[\frac{1}{[R^2+(D-L/2)^2]^{3/2}} - \frac{1}{[R^2+(D+L/2)^2]^{3/2}}\right]} \tag{51}$$

with

$$\mathcal{A} = NI = Jt_r L. \tag{52}$$

For equal current directions, the force on each coil points toward the other coil. The two forces have equal magnitude and opposite direction,

$$\boldsymbol{F}_1 = -\boldsymbol{F}_2, \tag{53}$$

which provides a useful consistency check for the OPERA calculation.

When the center separation is much larger than both the solenoid radius and length,

$$D \gg R, \qquad D \gg L, \tag{54}$$

each solenoid behaves as a magnetic dipole. Expanding Eq. (51) for large D gives

$$|F_z(D)| \simeq \frac{3\mu_0 \pi \mathcal{A}^2 R^4}{2D^4}. \tag{55}$$

Since the dipole moment of each identical coil is

$$m = \mathcal{A}\pi R^2 = NI\pi R^2, \tag{56}$$

Eq. (55) may also be written as

$$|F_z(D)| \simeq \frac{3\mu_0 m^2}{2\pi D^4}. \tag{57}$$

The D^{-4} dependence is the expected axial force law for two magnetic dipoles. It explains the rapid decrease in interaction force as the center-to-center separation increases.

The formulation also gives the expected current scaling,

$$F_z \propto \mathcal{A}_1 \mathcal{A}_2 \propto J_1 J_2. \tag{58}$$

For two identical coils carrying equal current density,

$$F_z \propto J^2. \tag{59}$$

Doubling both current densities therefore increases the force magnitude by a factor of four, while reversing one current reverses the force direction. These symmetry, direction, distance, and current-scaling properties are used as checks on the corresponding OPERA two-solenoid force calculation.

2.4 Numerical Finite-Thickness Two-Solenoid Force Construction

The numerical formulation follows the same mutual-inductance framework developed in Sec. 2.3, but departs from the analytical derivation at the point where the receiving solenoid is replaced by a magnetic dipole. Rather than introducing the small-solenoid approximation, both windings are retained as finite-thickness distributions of coaxial

circular current filaments. The force is then obtained by numerically integrating the exact filament–filament interaction over the complete radial–axial cross sections of the two coils.

For a homogenized winding with uniform azimuthal engineering current density J_i, a differential element of its cross section carries the filament current

$$\mathrm{d}I_i = J_i \,\mathrm{d}r_i \,\mathrm{d}\zeta_i, \tag{60}$$

where r_i is the filament radius and ζ_i is its axial position relative to the center of coil i. The signed separation between a filament in coil 1 and a filament in coil 2 is

$$s = D + \zeta_2 - \zeta_1, \tag{61}$$

where D is the center-to-center separation defined in Eq. (33).

The mutual inductance of each filament pair is evaluated using the Maxwell–Grover expression given in Eq. (40), with the fixed mean radii R_1 and R_2 replaced by the local filament radii r_1 and r_2. The corresponding elliptic parameter is therefore obtained from the same definition used previously, evaluated locally as

$$k^2 = \frac{4r_1 r_2}{(r_1+r_2)^2+s^2}. \tag{62}$$

At fixed filament currents, the axial interaction force follows directly from the mutual-inductance force relation in Eq. (38). For a differential filament pair,

$$\mathrm{d}F_z = \mathrm{d}I_1 \,\mathrm{d}I_2 \,\frac{\partial M_{\mathrm{loop}}}{\partial s}. \tag{63}$$

Substituting Eq. (60) and integrating over the complete cross sections of both windings gives

$$\begin{aligned} F_z(D) = J_1 J_2 \int_{r_{\mathrm{in},1}}^{r_{\mathrm{out},1}} \int_{-L_1/2}^{L_1/2} \int_{r_{\mathrm{in},2}}^{r_{\mathrm{out},2}} \int_{-L_2/2}^{L_2/2} \\ \times \frac{\partial M_{\mathrm{loop}}}{\partial s}(r_1, r_2, D+\zeta_2-\zeta_1)\,\mathrm{d}\zeta_2\,\mathrm{d}r_2\,\mathrm{d}\zeta_1\,\mathrm{d}r_1. \end{aligned} \tag{64}$$

Equation (64) is evaluated using tensor-product Gauss–Legendre quadrature in the radial and axial directions. The discrete approximation is

$$F_z \approx J_1 J_2 \sum_{a,b,c,d} w_{r_1,a}\, w_{\zeta_1,b} w_{r_2,c} w_{\zeta_2,d} \left.\frac{\partial M_{\mathrm{loop}}}{\partial s}\right|_{r_{1,a},\, r_{2,c},\, s=D+\zeta_{2,d}-\zeta_{1,b}}, \tag{65}$$

where the w terms are the mapped quadrature weights. The calculation is repeated with progressively larger numbers of radial and axial nodes until the resulting force changes negligibly, providing a direct numerical convergence check.

This construction therefore extends the analytical formulation without changing its underlying mutual-inductance basis. The reduced-order method continues from Eq. (43) by replacing one winding with a magnetic dipole, whereas the numerical method retains both finite windings and evaluates their interaction directly. It therefore avoids the point-dipole, mean-radius, and large-separation approximations and remains applicable when the coil dimensions are comparable to their separation.

The remaining assumptions are axisymmetry, uniform homogenized current density, rigid windings, and an air- or vacuum-core environment. For two isolated coils, the calculated forces must satisfy

$$\boldsymbol{F}_1 = -\boldsymbol{F}_2, \tag{66}$$

providing a consistency check for comparison with the OPERA conductor-force integration.

2.5 Optimized-Model Electromagnetic Force Framework

The force analysis of the optimized FCC-ee magnet focuses on the conductor-level axial loads produced by the complete main- and screening-solenoid system. Unlike the reduced two-solenoid benchmark, the optimized model contains many closely spaced conductors with different dimensions, axial positions, and current densities. The force on each screening segment therefore results from the superposed interaction with the main solenoid and every other screening conductor.

For an axisymmetric winding carrying azimuthal engineering current density J_ϕ, the axial Lorentz-force density is

$$f_z = -J_\phi B_r, \tag{67}$$

where B_r is the radial magnetic field acting within the conductor. The axial force on conductor i is consequently

$$F_{z,i} = -2\pi \int_{z_{i,\min}}^{z_{i,\max}} \int_{r_{i,\min}}^{r_{i,\max}} J_{\phi,i}\,(r,z) B_{r,i}^{\mathrm{ext}}(r,z)\, r\,\mathrm{d}r\,\mathrm{d}z, \tag{68}$$

where $B_{r,i}^{\mathrm{ext}}$ is the radial field generated by all sources other than conductor i. Excluding the target conductor's own field isolates its net translational force from the internal magnetic stress within the winding.

An independent analytical reconstruction is used to evaluate the coil-only force distribution of the optimized system. Each finite-thickness conductor is discretized into equivalent circular current loops. A source cell s with radial and axial dimensions Δr_s and Δz_s carries the equivalent loop current

$$I_s = J_{\phi,s}\Delta r_s \Delta z_s. \tag{69}$$

The external radial field acting on conductor i is reconstructed from all loops belonging to the remaining conductors,

$$B_{r,i}^{\mathrm{ext}}(r,z) = \sum_{\substack{k=1 \\ k\neq i}}^{N_{\mathrm{cond}}} \sum_{s\in k} B_r^{\mathrm{loop}}(r,z;a_s,z_s,I_s), \tag{70}$$

where a_s and z_s are the radius and axial position of source loop s. The reconstructed field is integrated over the target winding to give

$$F_{z,i}^{\mathrm{analytical}} = -\sum_{q\in i} J_{\phi,i}\, B_{r,i}^{\mathrm{ext}}(r_q,z_q)\Delta V_q, \tag{71}$$

with

$$\Delta V_q = 2\pi r_q \Delta r_q \Delta z_q. \tag{72}$$

The source and target discretizations are refined until the calculated conductor forces converge. This calculation provides a model-independent reference for the mutual coil–coil loading and allows the numerical performance of the complete OPERA force extraction to be assessed at the individual-conductor level.

The optimized geometry is evaluated in two otherwise identical OPERA models. The full model retains the nonlinear magnetic properties of the detector yoke and calorimeter. In the reference model, the same material bodies remain in the same positions, but their relative permeabilities are set to unity. All coil currents, conductor geometries, boundaries, symmetry conditions, and force-integration settings are left unchanged.

The $\mu_r = 1$ model establishes a controlled nonmagnetic reference in which the conductor forces arise only from the prescribed coil system. Retaining the material volumes ensures that the geometric model, finite-element domain, and numerical extraction procedure remain matched to the full-material case. The analytical coil-only reconstruction can therefore be compared directly with

$$F_{z,i}^{\mathrm{OPERA},\mu_r=1}, \tag{73}$$

providing an independent test of both the equivalent-loop calculation and the OPERA conductor-force integration. An additional benefit of this matched reference model is that the effect of the magnetized materials can be isolated and tabulated through direct comparison with the full nonlinear-material solution.

Agreement is assessed using the parity relation

$$F_{z,i}^{\mathrm{OPERA},\mu_r=1} = aF_{z,i}^{\mathrm{analytical}} + b, \tag{74}$$

for which ideal performance corresponds to

$$a = 1, \qquad b = 0, \qquad R = 1, \tag{75}$$

where R is the linear correlation coefficient. The slope identifies any systematic multiplicative difference, the intercept tests for a uniform offset, and the correlation measures how accurately the conductor-to- conductor force pattern is reproduced. Absolute residuals are used near force zero crossings, where percentage differences become ill-conditioned.

Once the coil-only calculation has been validated, the contribution of the ferromagnetic detector components is isolated by subtracting the nonmagnetic solution from the full nonlinear OPERA result,

$$\Delta F_{z,i}^{\mathrm{material}} = F_{z,i}^{\mathrm{OPERA,full}} - F_{z,i}^{\mathrm{OPERA},\mu_r=1}. \tag{76}$$

This difference represents the position-dependent change in conductor force caused by flux redistribution, magnetic shielding, and local saturation in the yoke and calorimeter. It is an additive, geometry-dependent correction rather than a simple scaling by relative permeability.

The independently reconstructed force may then be combined with this material contribution according to

$$F_{z,i}^{\mathrm{analytical,corr}} = F_{z,i}^{\mathrm{analytical}} + \Delta F_{z,i}^{\mathrm{material}}. \tag{77}$$

Comparison of $F_{z,i}^{\mathrm{analytical,corr}}$ with the full nonlinear OPERA result tests whether the complete conductor-force distribution can be interpreted as the sum of a validated coil-only interaction and a material-induced correction.

Because the optimized screening system is mirror symmetric, the signed global force may approach zero even when substantial loads act on individual conductors. The overall internal loading is therefore characterized using the cumulative absolute screening force,

$$\mathcal{L}_{\mathrm{abs}} = \sum_{i\in\mathrm{screen}} \left|F_{z,i}\right|. \tag{78}$$

This quantity prevents opposing mirror loads from canceling and provides a more representative measure of the axial force that must ultimately be transmitted through the winding supports. The optimized-model analysis therefore evaluates not only global equilibrium, but also the conductor-level force pattern, analytical–numerical agreement, and the additional loading introduced by the nonlinear magnetic materials.

3 Experimental Methods

3.1 Solenoid Fitting and Differential-Evolution Optimization

The optimization begins by evaluating the main-solenoid field using the finite-thickness analytical model described in Sec. 2. In the fixed-main mode used for the present study, the main-solenoid geometry remains unchanged and its current density is either prescribed or scaled to produce the requested central field. In the optional fitted-main mode, Differential Evolution first determines a main-solenoid geometry that approximates the prescribed Gaussian central profile within the specified geometric bounds.

The required screening interval is determined from the axial extent of the main-solenoid fringe field. Beginning outside the protected central region, the outer boundary is defined by the position at which the main-solenoid field falls below the prescribed tail tolerance. The resulting interval specifies the region to be covered by the screening system, subject to the computational domain, screening-coil envelope, and geometric safety margins.

The screening system consists of two mirror-symmetric chains of contiguous finite-thickness solenoid segments positioned on opposite sides of the magnetic center. The chains share a common radial cross-section and segment-length distribution, while their axial coordinates are related by reflection. Primary screening segments are constrained to oppose the main-solenoid fringe field. Optional trim segments may subsequently be permitted to carry either current sign to reduce small residual oscillations.

Differential Evolution optimizes the nonlinear screening-chain geometry, including the common inner radius, radial thickness, axial starting position, number of active segments, and relative segment lengths. The decoded segment lengths tile the required cancellation interval without gaps or overlaps while satisfying the prescribed length bounds. Candidate geometries that violate the bore clearance, radial limits, axial envelope, or spacing requirements receive a large objective penalty.

For each candidate geometry, the unit-current field kernels of the screening segments are evaluated on the axial grid and assembled into a response matrix. The segment current densities are then obtained through the bounded weighted least-squares solution of Eq. (9), rather than being searched directly by Differential Evolution. The regional weights prioritize central-field preservation, suppression near the target cutoff, cancellation of the main-solenoid wing, and reduction of the far-field residual.

The resulting field is assessed using the weighted objective function of Eq. (7). Differential Evolution searches the geometric parameter space over multiple population restarts, after which the best candidate may be refined using bounded local minimization. Because the current densities are re-solved within every objective evaluation, each trial geometry is evaluated using its own optimal bounded current distribution.

The screening-chain resolution is increased adaptively. The procedure begins with a limited segment count and optimizes the complete chain at that resolution. If the field-quality or coverage requirements are not satisfied, the segment containing the largest weighted residual is subdivided. The resulting configuration seeds the next optimization, during which all segment dimensions, positions, and current densities are re-optimized. Refinement is therefore concentrated where the target field is most difficult to reproduce, rather than being introduced as a fixed correction to the preceding solution.

This process continues until the required transition and wing metrics are satisfied, the maximum permitted segment count is reached, or further subdivision produces negligible improvement. Optional signed trim segments are then tested at the outer end of the primary chain. When accepted, their current densities are solved simultaneously with those of the primary segments so that the complete screening system remains globally optimized.

After the final configuration is selected, the magnitudes of the primary segment current densities are fitted to

$$|J(s)| = J_{\mathrm{floor}} + A\exp(-ks), \tag{79}$$

where s is a normalized coordinate along the screening chain. This fit is used only to characterize the spatial trend of the optimized current distribution and is not imposed during the inverse optimization.

The final solution is assembled from the main-solenoid field, the individual screening-segment fields, the combined screening field, and the optimized total field. Global and region-specific performance measures are then evaluated, including the total root-mean-square error, cancellation- and transition-region errors, wing error, maximum outer residual, and uncovered cancellation length. The optimized geometry and current densities are exported as parameter tables and OPERA-3D conductor definitions, together with numerical field arrays, convergence histories, adaptive-refinement logs, diagnostic summaries, and multipage reports. These outputs provide both a realizable magnet description for finite-element validation and a detailed record of the optimized fringe-field-cancellation performance.

3.2 Analytical and Numerical Two-Solenoid Validation

Before the force-extraction procedure was applied to the complete optimized magnet, it was tested using a reduced system consisting of two identical coaxial solenoids. This benchmark isolated the electromagnetic interaction between current-carrying windings without introducing ferromagnetic materials, structural components, gravitational loading, or mechanical supports.

Both solenoids were assigned the same inner radius, outer radius, axial length, and uniform engineering current density. One solenoid remained fixed, while the second was translated along the common axis over a sequence of center-to-center separations. The scan covered both the near-field region, where the winding dimensions are comparable to the separation, and the far-field region, where the magnetic field varies more gradually across the moving coil.

A MATLAB workflow was used to evaluate two independent theoretical force models at each separation. The first was the reduced-order finite-solenoid approximation developed in Sec. 2.3. In this model, the fixed winding was retained as a finite source solenoid, while the moving winding was represented by its magnetic dipole moment. This calculation provided a simple analytical reference and reproduced the expected large-separation behavior.

The second model used the finite-thickness numerical construction described in Sec. 2.4. Each rectangular winding cross-section was represented by Gauss–Legendre quadrature points in the radial and axial directions. The quadrature points acted as equivalent circular current filaments whose currents were determined by the local quadrature weights and the prescribed engineering current density. The exact coaxial-loop interaction was evaluated for every filament pair, and the total axial force was obtained by summing the weighted contributions over both windings. Several quadrature orders were evaluated to verify numerical convergence.

For every selected geometry, the same MATLAB workflow recorded the moving-coil position, center separation, surface gap, and force predicted by both theoretical models. It also generated the corresponding OPERA conductor definitions, ensuring that the analytical, numerical, and OPERA calculations used identical winding dimensions, positions, and current densities.

Each geometry was then solved as a magnetostatic OPERA-3D model using two complete Biot–Savart solenoid conductors. The force and torque on both windings were extracted in the OPERA Post-Processor using the conductor-force integral. The magnitude of the axial OPERA force was compared independently with the reduced-order analytical result and the finite-thickness numerical result at every separation.

The comparison was evaluated using the overall force trend, the point-by-point relative difference from OPERA, and the behavior of each theoretical model as the separation increased. The forces on the two conductors were also summed to verify that OPERA produced equal and opposite axial loads with negligible transverse force and numerical residual.

This benchmark established the physical and numerical consistency of the OPERA conductor-force calculation before the same extraction procedure was applied to the full optimized screening-solenoid system.

3.3 Full-Model OPERA Force Determination and Material-Isolation Workflow

The validated force-extraction procedure was applied to the complete optimized detector-magnet model at nominal current. The model contained one main solenoid, 318 screening solenoids arranged as 159 mirror pairs, and nonlinear magnetic regions representing the detector yoke and calorimeter.

Force and torque vectors were extracted for all 319 conductors and associated with their geometry, current density, ampere-turns, volume, axial position, and mirror-partner identification. Because conductors on opposite sides of the magnetic center used opposite local orientations, the reported axial-force components were transformed to a common global sign convention. Positive-z conductors retained the OPERA sign, whereas the signs of the negative-z conductors were reversed. The original OPERA values were also retained for traceability.

The processed conductor dataset was used to calculate the axial-force distribution, force magnitude, force per unit conductor volume, and force per unit axial length. The screening conductors were ranked by force magnitude. Mirror-pair residuals, side-specific force sums, and the signed global force balance were evaluated as consistency measures. The cumulative absolute screening load was calculated by summing the magnitudes of the individual screening-conductor forces.

An independent coil-only force reconstruction was performed in MATLAB. Each finite-thickness solenoid was discretized into equivalent circular current loops, with each loop current determined from the engineering current density and the associated source-cell area. For every target winding, the radial magnetic field generated by all other conductors was evaluated over a radial–axial integration grid. Source loops belonging to the target conductor were excluded, and the resulting axial Lorentz-force density was integrated over the complete target-winding volume. The source and target discretizations were successively refined to assess numerical convergence.

The reconstructed coil-only forces were compared with the conductor forces extracted from the nominal nonlinear-material OPERA model. To establish a matched coil-only finite-element reference, a second OPERA model was generated in which the yoke and calorimeter geometries were retained but their relative permeabilities were set to unity. The conductor definitions, current densities, boundary conditions, symmetry conditions, solver settings, and force-extraction procedure were otherwise unchanged.

The nonmagnetic model was solved independently, and the conductor forces were processed using the same global sign convention. The material-induced force contribution for each conductor was defined as the difference between the full-material and nonmagnetic OPERA forces. This conductor-specific additive correction was subsequently combined with the independently reconstructed coil-only force.

Three force comparisons were constructed: the analytical coil-only forces against the full-material OPERA forces, the analytical coil-only forces against the nonmagnetic OPERA forces, and the material-corrected analytical forces against the full-material OPERA forces. Each comparison was evaluated using linear-fit slopes and intercepts, correlation coefficients, signed residuals, absolute residuals, and percentage differences. Percentage differences were excluded near force zero crossings, where normalization by a small reference value becomes ill-conditioned.

The position dependence of the material contribution was characterized using both the additive force correction and the ratio of the full-material force to the nonmagnetic force. The additive correction was used as the primary quantity, while the force ratio was retained as a secondary diagnostic away from zero crossings. The cumulative absolute screening loads from the full-material and nonmagnetic models were also calculated for system-level comparison.

The nonlinear B–H data for the yoke and calorimeter were converted to SI units and processed to examine their field-dependent magnetic response. The resulting material-property data were compared with the conductor-force corrections to support interpretation of the spatially varying material contribution without assuming a direct permeability-based force multiplier.

All conductor-force datasets, material corrections, and comparison metrics were exported to spreadsheet and comma-separated formats. The analysis outputs included force-versus-position curves, parity comparisons, residual distributions, material-correction profiles, cumulative-load summaries, and multipage reports for the full-material, nonmagnetic, and corrected force datasets.

4 Experimental Results and Data Analysis

4.1 Magnetic Field Optimization Results

The production calculation was performed in the fixed-main operating mode described in Sec. 3.1. In this configuration, the geometry of the main solenoid is prescribed, while the geometry and current distribution of the mirror-symmetric screening chains are optimized. The complete production inputs are listed in Table A1 of Appendix A. The principal field-quality metrics are summarized in Table B1 of Appendix B, while the final main-solenoid and screening-chain parameters are reported in Tables C1 and C2 of Appendix C.

The production optimization converged to a mirror-symmetric configuration with 24 primary screening segments on each side and no accepted signed trim segments. Figure 1 compares the target profile defined in Eq. (1), the fixed main-solenoid field, the combined screening field, and the optimized total field of Eq. (2).

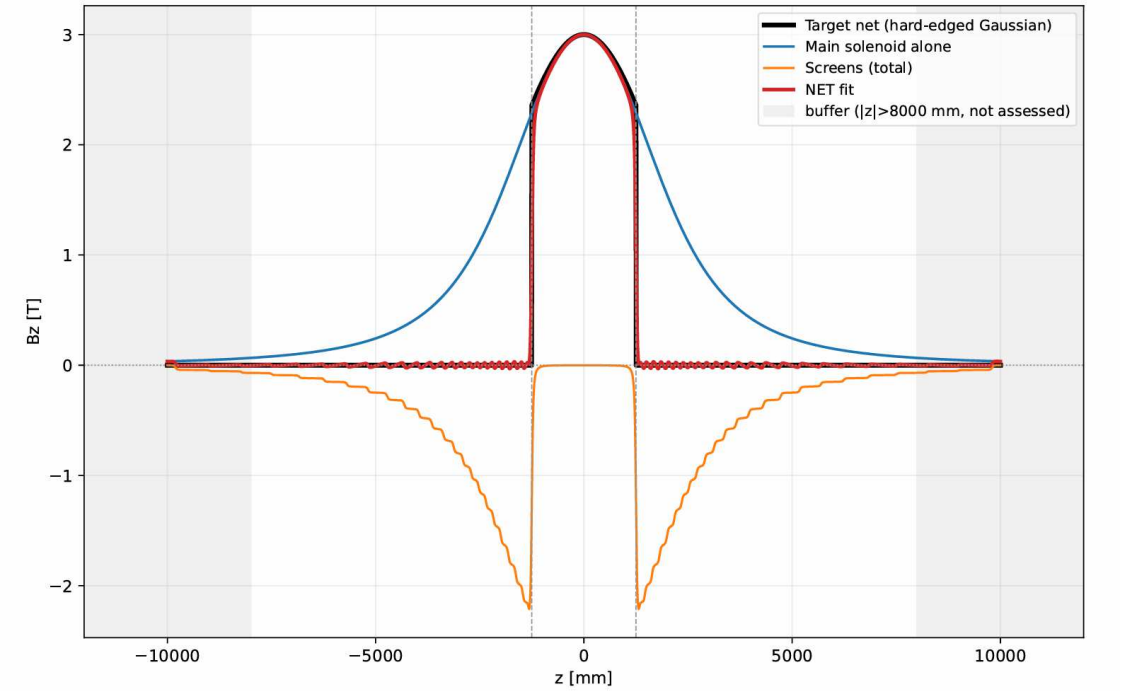


Figure 1: Optimized reconstruction of the prescribed hard-edged axial magnetic-field profile. The fixed main-solenoid field is combined with the total field of the two segmented screening chains. The optimized total field preserves the central Gaussian-like peak while strongly suppressing the extended main-solenoid fringe field. Vertical dashed lines indicate the prescribed cutoff positions, and the shaded regions outside $|z| = 8000$ mmdenote the endpoint buffer excluded from the primary field-quality assessment.

The main solenoid alone produces a broad axial field with a substantial fringe component outside the protected interval. The screening system generates an opposing field that remains comparatively small near the center but grows rapidly in magnitude near the prescribed cutoff. Their superposition preserves the central field while suppressing most of the main-solenoid tail throughout the assessed external region.

The optimized peak field is 2.9994 T, corresponding to an error of approximately -0.02% relative to the prescribed 3.0 T peak. The near-peak root-mean-square error is 4.05×10^{-3} T, demonstrating that the screening chains introduce only a small perturbation to the useful central field. The combined center-and-wing RMSE is 2.49×10^{-2} T. Thus, the optimization successfully separates the two principal requirements of the inverse-design problem: preservation of the detector field and suppression of the extended fringe field. The residual defined in Eq. (6) is shown in Fig. 2.

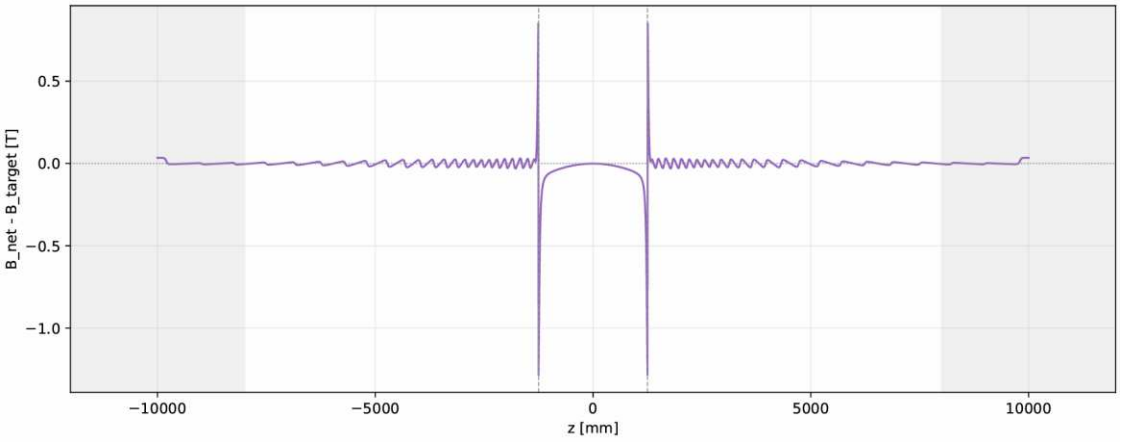


Figure 2: Residual field, $B_{total} - B_{target}$, as defined in Eq. (6). The largest excursions occur at the discontinuous target-field cutoffs. Away from these transitions, the remaining error consists primarily of lower-amplitude oscillations associated with the finite segmentation of the screening chains. The shaded endpoint regions lie outside the assessed interval.

The largest residual excursions occur at the prescribed cutoff positions. This concentration of error follows directly from the idealized discontinuity in Eq. (1): the target falls instantaneously to zero, whereas the finite-thickness solenoidal fields of Eq. (3) remain continuous. The optimized field therefore approximates the hard edge through a rapid but finite transition.

Within the protected interval, the residual remains small relative to the 3 T field scale and is approximately symmetric about the magnetic center. Outside the cutoff, the residual alternates about zero. These oscillations arise from the superposition of a finite number of localized screening-segment fields and constitute the principal remaining error away from the discontinuous transition.

Within the assessed physical wing, $|z| \leq 8000$ mm, the residual field has an RMS value of 1.35×10^{-2} T and a maximum magnitude of 6.09×10^{-2} T. The far-wing RMS is 9.34×10^{-3} T, with a maximum far-wing residual of 2.35×10^{-2} T. The remaining wing error reflects the finite segmentation, the realizability constraints, and the competition among the region-dependent terms in the weighted objective of Eq. (7). Detailed transition- and far-wing performance metrics are provided in Appendix B

The screening segments share a common radial envelope but have independently optimized axial lengths and current densities while the main solenoid retains its prescribed geometry. The two chains are related by reflection about $z = 0$, as required by the symmetric target and optimization geometry.

The full geometric and electrical values are tabulated in Appendix C. The screening chains occupy the radial interval from 30 mm to 40 mm, substantially inside the main-solenoid inner radius. The segment centers extend from approximately 1288 mm to 9396 mm on each side. This geometry places the largest screening-current density close to the protected-field boundary while distributing progressively weaker corrections across the extended axial tail.

Fig. 3 shows the field produced by each segment and the cumulative field of each chain.

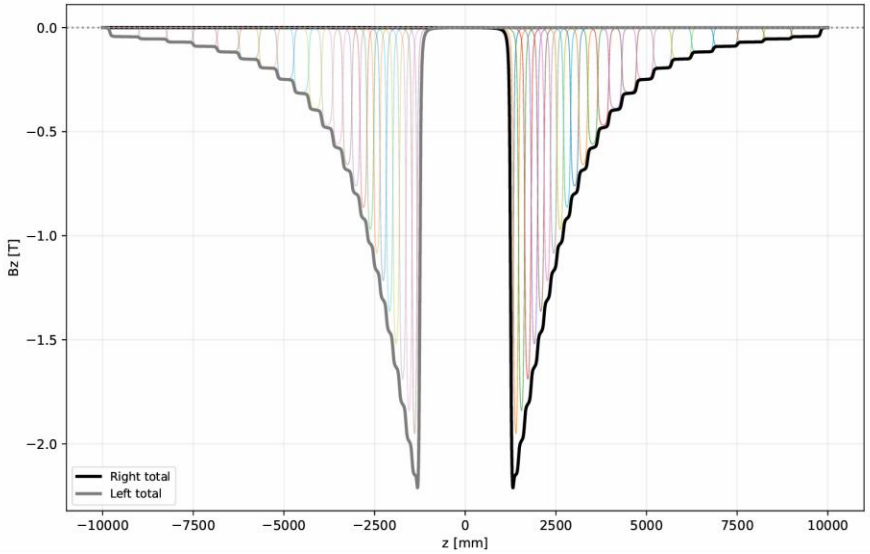
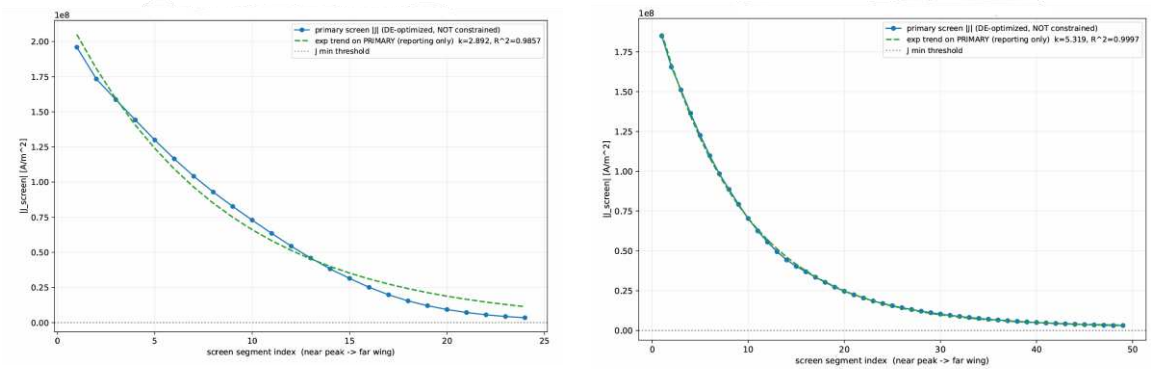


Figure 3: Individual axial-field contributions of the optimized screening segments. Thin curves show the field generated by each segment, while the thick black and gray curves show the cumulative right- and left-chain fields, respectively. Inner segments produce strong localized cancellation near the target cutoff, whereas outer segments provide weaker and broader correction of the far-field tail.

The detector-facing segments produce the strongest and most localized negative field contributions. These segments control the rapid collapse immediately outside the protected interval. With increasing distance from the detector, the individual fields become weaker and broader. The optimized current-density distribution is shown in Fig. 4, depicting the effect of increasing the number of segments.



Production solution with 24 segments per side.

Higher-resolution solution with 49 segments per side.

Figure 4: Optimized screening-current-density magnitude versus segment index for (a) the 24-segment production solution and (b) the 49-segment higher-resolution solution. The reporting-only exponential fits give $k = 2.892$, $R^2 = 0.9857$ and $k = 5.319$, $R^2 = 0.9997$, respectively. The dotted line marks the minimum accepted current-density magnitude.

The functional form of the currents is not prescribed during the bounded least-squares solution of Eq. (9). Nevertheless, both segmentation levels develop a smooth, approximately exponential decrease from the detector-facing region toward the far wing.

For the 24-segment production solution, the current-density magnitude decreases from approximately 1.96×10^8 A m^{-2} to 3.45×10^6 A m^{-2}. The reporting-only fit defined in Eq. (79) gives $R^2 = 0.9857$. The 49-segment comparison solution follows the exponential representation more closely, with $R^2 = 0.9997$. The increased agreement at finer segmentation suggests that the higher-resolution chain resolves a smooth axial current trend more faithfully, whereas the 24-segment design represents that trend using a coarser piecewise distribution. The exponential fits remain descriptive and are meant to show the natural progression of the current densities throughout the screening coils. The optimized segment lengths shown in Fig. 5 exhibit the complementary spatial trend.

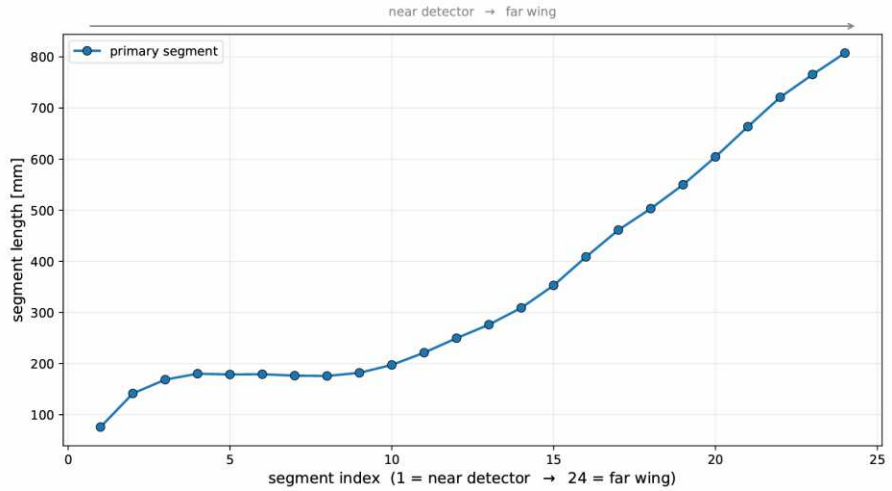


Figure 5: Optimized axial length of each primary screening segment. Segment 1 is nearest the detector and segment 24 is in the far wing. Short inner segments provide local control near the rapid target-field transition, whereas longer outer segments act on the more slowly varying fringe field.

The first segment is approximately 76 mm long. The segment lengths increase to approximately 175 mm across the inner portion of the chain, remain nearly constant over several intermediate segments, and then increase progressively through the outer half. The final segment reaches a length of approximately 808 mm. This variation is consistent with the adaptive-refinement strategy described in Sec. 3.1. Short segments provide additional spatial freedom where the target changes rapidly and the residual is most difficult to control. Longer segments are sufficient in the far wing, where the main-solenoid field varies over a larger axial scale.

The Differential-Evolution convergence history is shown in Fig. 6.

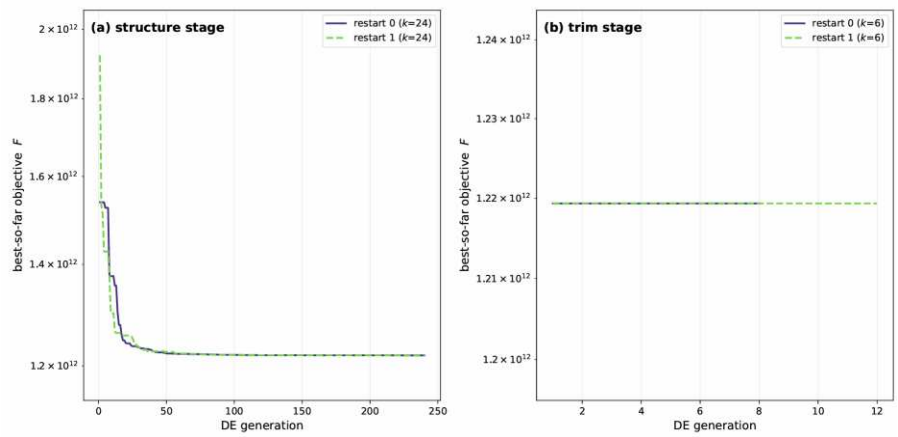


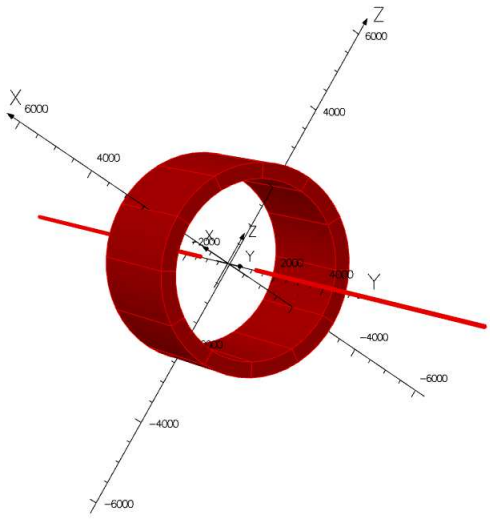
Figure 6: Differential-Evolution convergence history. Panel (a) shows the 24-segment primary structure search for two independent restarts. Panel (b) shows the subsequent six-position signed-trim search. The structure-stage restarts converge to closely matching objective values, while no accepted improvement is produced during the trim stage.

During the primary structure search, both independent restarts undergo a rapid initial reduction of the best-so-far objective. The objective decreases from approximately $1.5–1.9 \times 10^{12}$ to approximately 1.23×10^{12} over the first 30–50 generations. Both restarts then approach nearly the same asymptotic value, with comparatively little additional improvement after approximately 60 generations. The convergence of the two independent populations to closely matching objective values indicates consistency between the restarts for this production calculation.

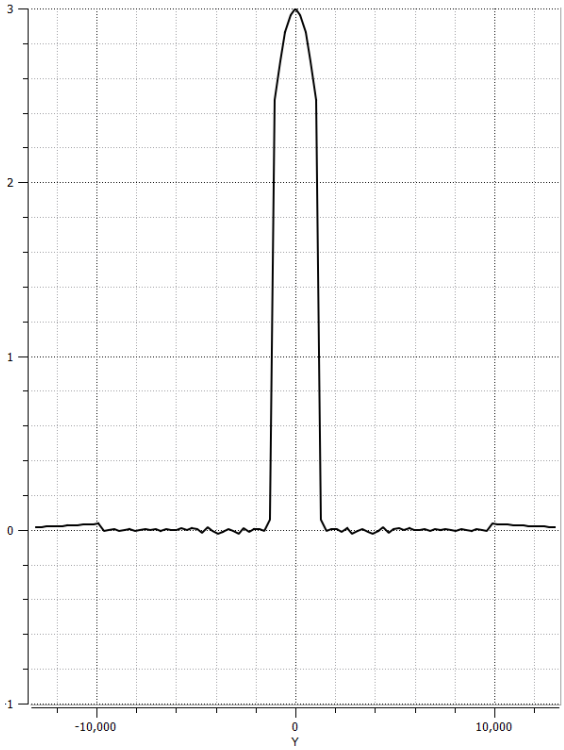
The signed-trim search remains nearly constant at approximately 1.219×10^{12} for both restarts. No trim configuration satisfies the acceptance criterion, and the final design therefore retains zero signed trim segments. Further improvement would instead require a change in the primary-chain spatial resolution, geometry bounds, current distribution, or objective trade-offs.

Because every optimized region is represented using the same finite-thickness solenoid model introduced in Sec. 2, the final geometry can be transferred directly into an OPERA-3D conductor description. The export contains the axial position, radial boundaries, axial length, current density, current direction, and winding parameters of the main solenoid and every screening segment.

The exported geometry was reconstructed in OPERA-3D, as shown in Fig. 7(a). The model reproduces the fixed main solenoid and both optimized screening chains using the final winding parameters listed in Appendix C. The corresponding on-axis field is shown in Fig. 7(b).



OPERA-3D finite-element reconstruction of the optimized 24-segment screening-solenoid geometry.



Corresponding on-axis magnetic field obtained from the OPERA-3D model.

Figure 7: OPERA-3D validation of the optimized screening system. Panel (a) shows the finite-element reconstruction of the fixed main solenoid and the two mirror-symmetric 24-segment screening chains using the dimensions and current densities reported in Appendix C. Panel (b) shows the resulting on-axis magnetic field. The finite-element solution preserves the approximately 3 T central field and reproduces the rapid suppression outside the protected interval, with only small residual variations across the external axial domain.

The OPERA-3D calculation preserves the central approximately 3 T field and reproduces the rapid suppression outside the protected interval. The external field remains close to zero over most of the modeled axial range, with small residual variations consistent with the finite segmentation of the screening system. This provides a qualitative finite-element validation of the exported inverse-designed geometry.

4.2 OPERA Two-Solenoid Force Validation

The OPERA conductor-force calculation was validated using two identical coaxial solenoids in air or vacuum. Restricting the benchmark to current-carrying windings removes the effects of nonlinear magnetic materials, structural components, gravity, and mechanical supports, allowing the OPERA results to be compared directly with the analytical and finite-thickness numerical force formulations developed in Secs. 2.3 and 2.4.

The benchmark geometry is summarized in Table 1. Coil 1 was fixed at $z_1 = -0.35$ m, while coil 2 was translated along the common axis. Both windings had identical rectangular radial–axial cross-sections and carried the same uniform engineering current density.

Table 1: Geometry and excitation used for the two-solenoid force benchmark.

Quantity	Symbol	Value
Inner radius	r_{in}	0.50 m
Outer radius	r_{out}	0.55 m
Mean radius	R	0.525 m
Radial thickness	t_r	0.050 m
Axial length	L	0.40 m
Uniform current density	J	1.0×10^7 A m^{-2}
Equivalent ampere-turns	$\mathcal{A} = Jt_rL$	2.0×10^5 A

Fixed-coil center	z_1	−0.35 m
Center separation	$D = z_2 - z_1$	0.60 m–12.35 m

Three independent force calculations were compared. The first was the OPERA Lorentz-force integration over the two Biot–Savart conductors, which directly evaluated the force exerted by each coil on the other. The second was the reduced-order analytical model developed in Sec. 2.3, in which coil 1 was retained as a finite source solenoid and coil 2 was approximated as a magnetic dipole located at its center. The third was the finite-thickness numerical formulation described in Sec. 2.4, which retained the full radial and axial dimensions of both windings.

The finite-thickness force formulation developed in Sec. 2.4 was evaluated using tensor-product Gauss–Legendre quadrature over the radial and axial dimensions of both windings. Quadrature orders of 8×12, 12×18, and 16×24 nodes per winding were tested. The 16×24 calculation provided the reported force, while comparison with the 12×18 result was used to verify numerical convergence.

In the OPERA coordinate convention used for this benchmark, the common solenoid axis corresponded to the global y direction. Equal current directions therefore produced a negative F_y on the moving coil, indicating attraction toward the fixed coil. Force magnitudes are used in the comparisons below.

For each theoretical method, the relative difference from OPERA was defined as

$$\epsilon_F = 100\,\frac{|F_{\text{method}}| - |F_{\text{OPERA}}|}{|F_{\text{OPERA}}|}. \tag{80}$$

A positive value of ϵ_F indicates that the comparison method predicts a larger force magnitude than OPERA. The complete force comparison is reported in Table 2, and the corresponding force trends are shown in Fig. 8.

Table 2: OPERA, reduced-order, and finite-thickness numerical force results. The relative differences are evaluated using Eq. (80).

D (m)	g (m)	|F_OPERA| (N)	|F_dip| (N)	|F_num| (N)	ε_dip (%)	ε_num (%)
0.60	0.20	26800.1277	35039.6800	26911.6000	30.74	0.416
0.75	0.35	16157.7419	22387.3200	16187.9000	38.55	0.187
0.95	0.55	8913.8528	12121.0500	8923.2400	35.98	0.105
1.20	0.80	4614.1144	5922.2670	4617.4300	28.35	0.072
1.50	1.10	2304.8353	2779.0390	2306.0800	20.57	0.054
1.85	1.45	1140.9588	1306.2100	1141.4500	14.48	0.043
2.35	1.95	487.8432	533.5461	488.0150	9.37	0.035
3.35	2.95	129.8489	135.9742	129.8880	4.72	0.030
5.35	4.95	21.1593	21.5427	21.1653	1.81	0.028
8.35	7.95	3.6476	3.6723	3.6487	0.68	0.028
12.35	11.95	0.7689	0.7707	0.7691	0.23	0.015

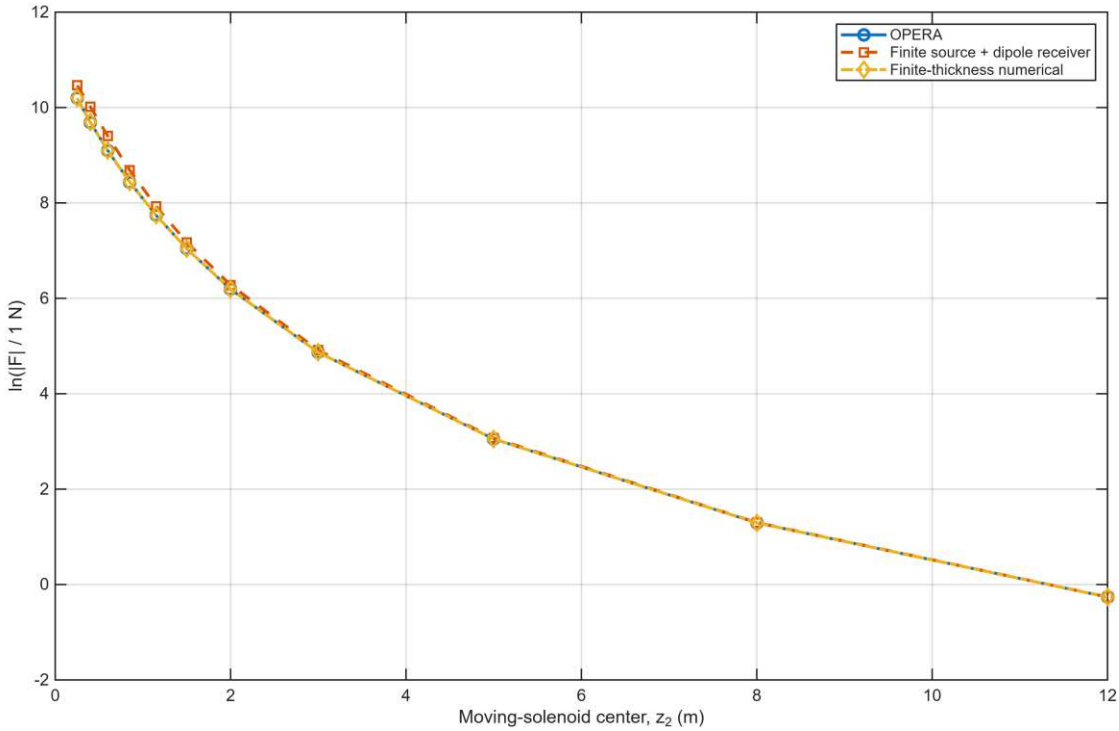
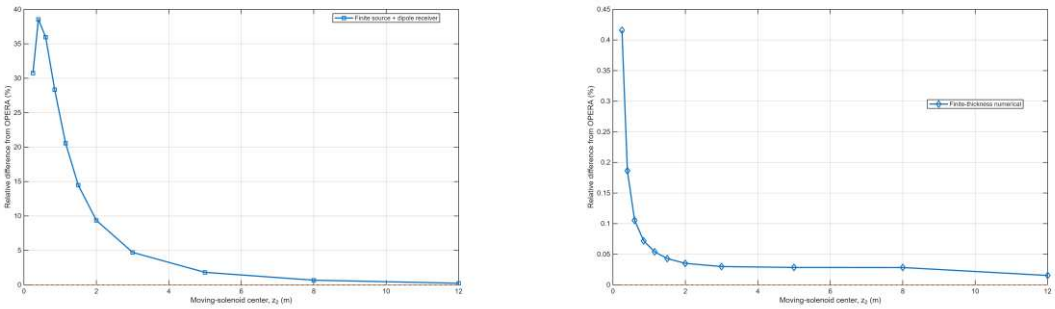


Figure 8: Natural logarithm of the force magnitude predicted by OPERA, the finite-source/dipole approximation, and the finite-thickness numerical calculation. Because $z_1$is fixed, increasing z_2 corresponds directly to increasing center separation $D = z_2 - z_1$.

As shown in Table 2 and Fig. 8, all three methods reproduce the rapid monotonic decrease in interaction force with increasing separation. The OPERA force decreases from approximately 2.68×10^4 N at $D = 0.60$ m to 7.69×10^{-1} N at $D = 12.35$ m, spanning more than four orders of magnitude.

The reduced-order dipole approximation systematically overpredicts the OPERA force at short and intermediate separations. In this model, the field gradient generated by the source solenoid is evaluated only at the center of the receiving coil. When the separation is comparable to the coil dimensions, the field varies appreciably across the receiving winding, and the center-point approximation does not represent the full volume-integrated interaction. The relative difference reaches approximately 38.6% and decreases steadily as the separation becomes large compared with the radial and axial dimensions of the coils. The relative differences shown in Fig. 9 demonstrate the substantially closer agreement obtained with the finite-thickness numerical calculation.



Finite-source/dipole approximation. Finite-thickness numerical calculation.

Figure 9: Relative differences between the two theoretical models and the OPERA force magnitude. Panel (a) shows the finite-source/dipole approximation, whose agreement improves progressively with increasing separation. Panel (b) shows the finite-thickness numerical calculation, which remains in close agreement with OPERA throughout the full separation scan.

Because this method resolves the radial and axial field variation throughout both winding cross-sections, its largest difference from OPERA is only approximately 0.42% at the closest separation. The difference falls below 0.1% by $D = 1.20$ m and reaches approximately 0.015% at the largest separation. The remaining deviations are

consistent with the finite quadrature order and the independent numerical field and force evaluations used by the two methods.

The OPERA solution also satisfied the expected action–reaction condition. At $D = 0.60$ m, the fixed and moving coils carried axial forces of approximately $+2.680012774 \times 10^4$ N and -2.680012770×10^4 N, respectively. Their summed residual was approximately 2.55×10^{-11} N, while the transverse force components were of order $\times 10^{-12}$ N or smaller.

These results demonstrate that the OPERA conductor-force calculation reproduces the expected force direction, action–reaction symmetry, and separation dependence of the idealized coaxial-solenoid system. The close agreement with the finite-thickness numerical calculation provides quantitative validation of the OPERA force extraction, while the reduced-order model independently confirms the expected asymptotic behavior at large separation.

4.3 Electromagnetic Force Study of the Optimized Solenoid Layout

Following validation of the force-extraction procedure with the reduced two-solenoid system, the analysis was extended to the complete optimized detector-magnet layout. The solved OPERA model contained the main detector solenoid, the full mirror-symmetric screening system, the nonlinear iron calorimeter, and the nonlinear return yoke. The complete model geometry is shown in Fig. 10, and its principal numerical properties are summarized in Table 3.

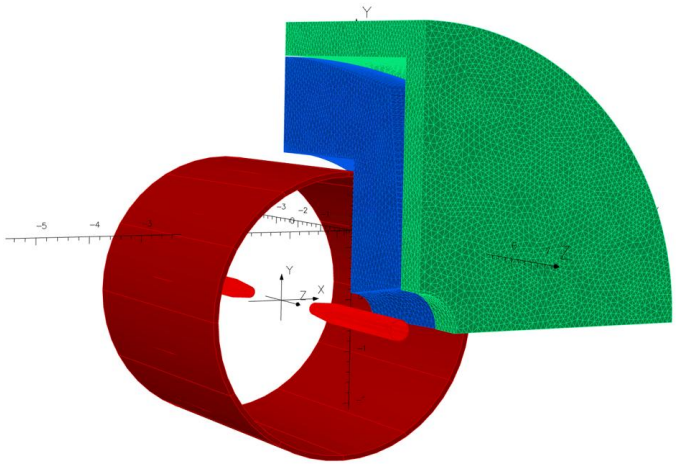


Figure 10: Optimized OPERA detector-magnet model containing the main solenoid, mirror-symmetric screening-solenoid system, iron calorimeter, and return yoke. The magnetic-material geometry is represented over the solved octant, while the Biot–Savart conductors represent the complete axisymmetric solenoids.

Table 3: Numerical description of the optimized OPERA model used for the electromagnetic-force study.

Quantity	Value
Analysis type	Nonlinear magnetostatic TOSCA
Stored operating case	Simulation 1, drive scaling factor 1.0
Biot–Savart conductors	319 complete solenoids
Main-solenoid conductors	1
Screening conductors	318, forming 159 mirror pairs
Mesh nodes	1,610,050
Tetrahedral elements	1,153,109
Magnetic materials	IRON_YOKE, IRON_CALORIMETER, and air
Solved geometric domain	One octant
Reflection symmetry	XY: inverse; YZ: positive; ZX: positive

The screening conductors shown in Fig. 10 are organized as mirrored pairs on opposite sides of the detector. Because the two members of each pair use opposite local cross-section orientations, the raw OPERA axial-force

component was converted to a common global convention. Forces on the positive-z conductors retain their reported sign, while those on the negative-z conductors are assigned the opposite sign. After this transformation, corresponding mirror conductors carry equal force magnitudes in opposite global axial directions.

The global axial-force distribution obtained from the complete nonlinear material model is strongly nonuniform. The detector-facing mirror pair, centered at $z = \pm 1.42$ m, carries the largest individual screening-conductor load, $|F_z|_{\max} = 1.294855 \times 10^4$ N.

The force decreases rapidly through the immediately adjacent conductors but does not vary monotonically over the complete screening chain. Several local force reversals occur, followed by a second broad load concentration near $|z| \simeq 2.8$ m. The largest force in this secondary region is approximately $|F_z| = 6.3656 \times 10^3$ N.

Beyond this region, the forces gradually decrease toward the outer end of the screening system. The complete full-material force distribution and the independent coil-only reconstruction are shown in Fig. 11.

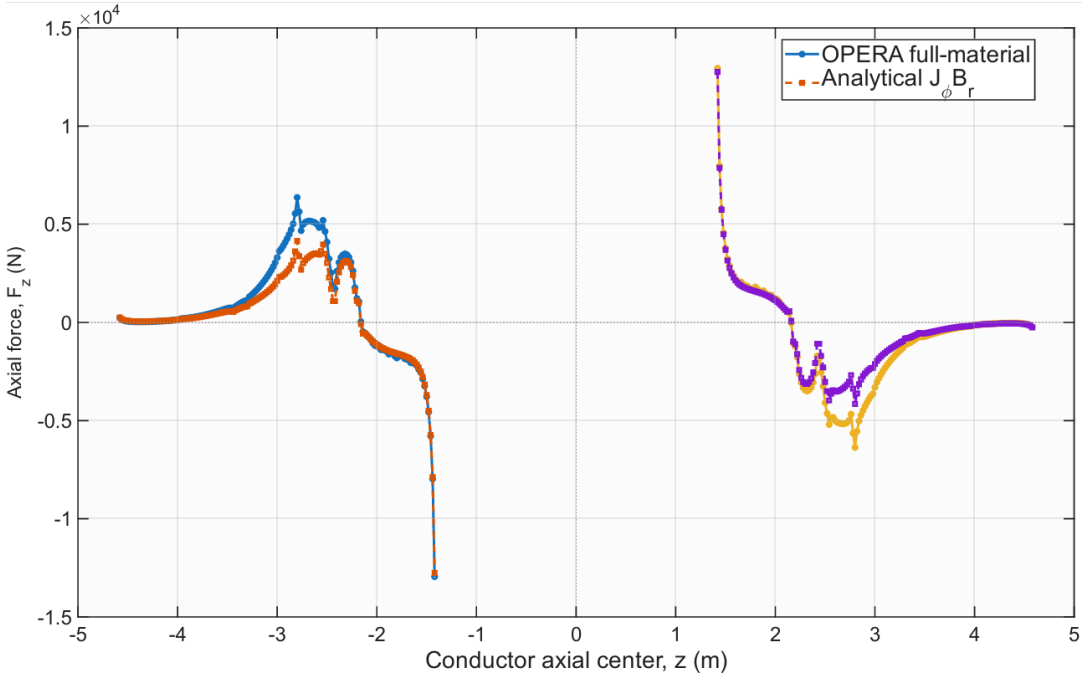


Figure 11: Full-material OPERA axial forces and the independent coil-only $J_\phi B_r$ reconstruction as functions of conductor axial position. The OPERA force profile contains a dominant detector-facing load, several force reversals, and a secondary concentration near $|z| = 2.8$ m. The systematic difference between the two curves is examined below by separating the ferromagnetic-material contribution.

The changes in force direction show that the screening chain cannot be characterized by a single resultant acting uniformly toward or away from the detector center. Each conductor interacts with the main-solenoid field, the remaining screening conductors, and the flux redistributed by the ferromagnetic detector components. The force distribution must therefore be examined conductor by conductor rather than inferred from the net force on the complete assembly.

The highest-loaded screening pairs are listed in Table 4. The two members of each pair have equal force magnitudes and opposite global axial directions.

Table 4: Highest-loaded screening mirror pairs in the full-material optimized magnet.

Conductor IDs	|z| (m)	R_mean (m)	|Fz| (N)	|Fz|/V (N m⁻³)
2/3	1.42	0.1015	12948.6	6.85109×10^7
4/5	1.44	0.1035	7968.97	4.12900×10^7
140/141	2.80	0.1755	6365.60	1.94667×10^7
6/7	1.46	0.1055	5792.65	2.94043×10^7
138/139	2.78	0.1755	5641.81	1.72532×10^7

The largest volume-averaged axial load is $\frac{|F_z|}{V} = 6.851087 \times 10^7$ N/m^3, and occurs in conductor 2 at $z = 1.42$ m. The same conductor also carries the largest integrated axial force. The force magnitude is not, however, determined by conductor radius alone. The dominant load occurs at a mean radius of 0.1015 m, whereas the second

major concentration occurs at a mean radius of 0.1755 m. Axial position, conductor dimensions, current density, local radial field, neighboring-coil interactions, and ferromagnetic flux redistribution all contribute to the final conductor load.

Although the individual conductor forces are substantial, the complete symmetric system has an essentially zero axial resultant. The positive- and negative-z screening chains carry equal and opposite summed loads of approximately -1.284698×10^5 N and $+1.284698 \times 10^5$ N, respectively. The cumulative absolute screening-conductor load is 6.055139×10^5 N, whereas the signed screening-force residual is only approximately -2.000001×10^{-5} N. The centered main solenoid has a calculated force magnitude of approximately 1.020480×10^{-8} N, and the complete-system axial residual is -1.999093×10^{-5} N. The corresponding normalized global imbalance is only 3.301481×10^{-11}. These results demonstrate that a nearly zero global force does not imply negligible internal loading. More than 600 kN of cumulative absolute axial force is distributed among the screening conductors, but the mirror-symmetric contributions cancel in the complete system. Across the 159 screening mirror pairs, the maximum absolute force residual was 2.0×10^{-5} N, while the RMS residual was 1.586103×10^{-6} N. The corresponding maximum relative mismatch was 6.563728×10^{-9}.

These residuals are many orders of magnitude smaller than the individual conductor forces and confirm that the transformed force data preserve the reflection symmetry of the model to numerical precision. The principal full-material force metrics are summarized in Table 5.

Table 5: Principal full-material conductor-force metrics for the optimized magnet.

Metric	Value
Maximum screening $\lvert F_z \rvert$	1.294855×10^4 N
Position of maximum screening load	$\lvert z \rvert = 1.42$ m
Sum of absolute screening forces	6.055139×10^5 N
Positive-side screening-force sum	-1.284698×10^5 N
Negative-side screening-force sum	$+1.284698 \times 10^5$ N
Net screening axial force	-2.000001×10^{-5} N
Main-solenoid force magnitude	1.020480×10^{-8} N
Total-system axial residual	-1.999093×10^{-5} N
Normalized global imbalance	3.301481×10^{-11}
Maximum $\lvert F_z \rvert / V$	6.851087×10^7 N m^{-3}
Maximum mirror-pair residual	2.000000×10^{-5} N
RMS mirror-pair residual	1.586103×10^{-6} N
Maximum relative pair mismatch	6.563728×10^{-9}

An independent force calculation was performed to verify the OPERA conductor-force extraction. Each finite solenoid was represented by a collection of equivalent circular current loops. The radial field generated by all other conductors was evaluated throughout each target winding, and the axial force was obtained by integrating the local $J_\phi B_r$ force density over the conductor volume. The self-field of the target conductor was excluded from its net translational-force calculation.

When this coil-only reconstruction was compared directly with the original full-material OPERA solution, the force directions and principal load concentrations were reproduced, but the analytical values were systematically smaller. The parity fit was

$$F_z^{\text{analytical}} = 0.784182\, F_z^{\text{OPERA,full}} + 4.932 \times 10^{-8} \text{ N},$$

with a correlation coefficient of $R = 0.98091642$.

The near-zero intercept and high correlation showed that the analytical model captured the conductor-interaction pattern, while the slope indicated a systematic difference in force magnitude. This comparison is shown in Fig. 12.

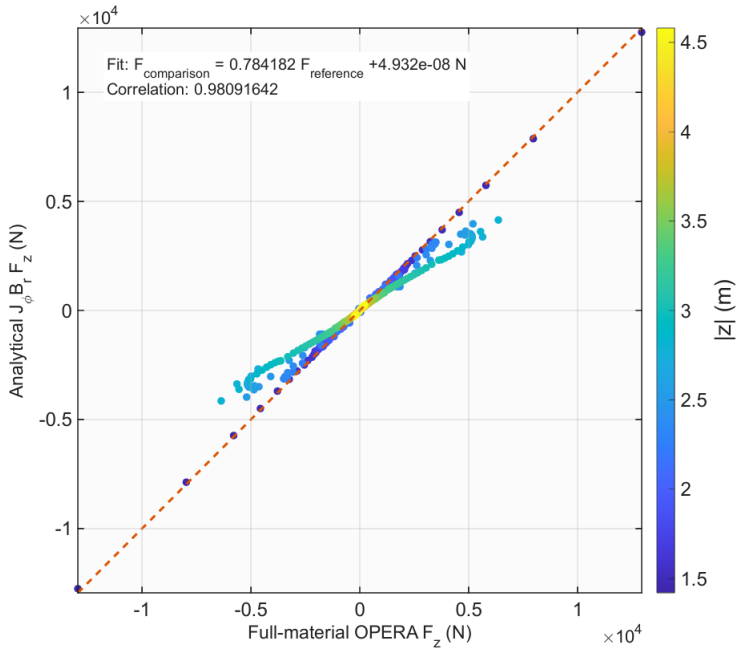


Figure 12: Parity comparison between the coil-only analytical reconstruction and the full-material OPERA result. The analytical calculation reproduces the global force pattern but underpredicts the force magnitude because it does not include the nonlinear yoke and calorimeter response.

To isolate the contribution of the ferromagnetic detector materials, the full-material OPERA results were compared with the matched $\mu_r = 1$ reference model described in Sec. 3.3.

The cumulative absolute screening load decreased from 6.055139×10^5 N in the full-material model to 4.751762×10^5 N in the nonmagnetic model. The difference is 1.303377×10^5 N, corresponding to a global absolute-load factor of

$$\frac{\Sigma_i \left| F_{z,i}^{\mathrm{OPERA,full}} \right|}{\Sigma_i \left| F_{z,i}^{\mathrm{OPERA},\mu_r=1} \right|} = 1.274293.$$

The nonlinear yoke and calorimeter therefore increase the cumulative absolute screening-conductor loading by approximately 27.4293 %. The largest material-induced force change occurs for conductors 138 and 139, centered at $z = \pm 2.78$ m. For these conductors, the absolute material correction is approximately

$$\left| \Delta F_z^{\mathrm{material}} \right| \simeq 2.2591 \times 10^3 \text{ N}.$$

The position of this maximum corresponds to the secondary load concentration identified in the full-material conductor-force distribution. The conductor-specific material correction is shown in Fig. 13.

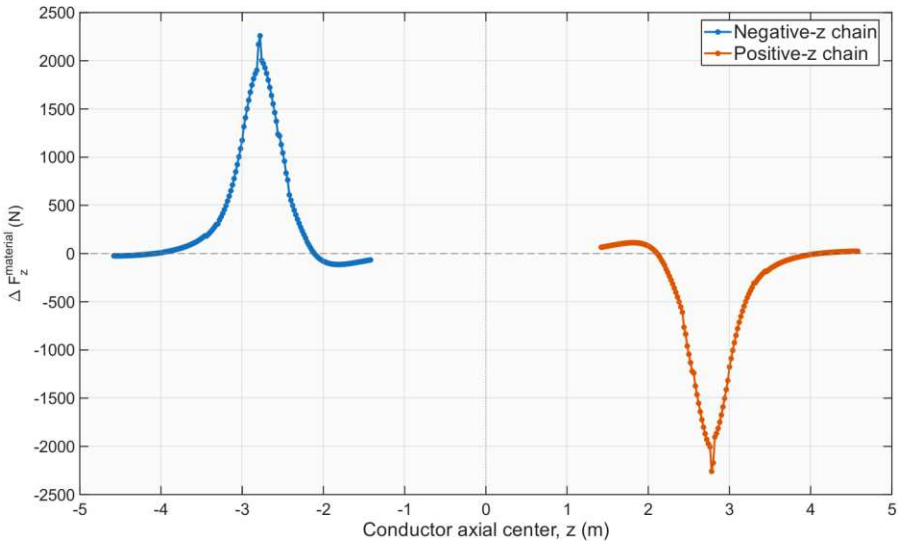


Figure 13: Conductor-specific ferromagnetic force correction, defined as the difference between the full-material and $\mu_r =$ 1OPERA solutions. The correction is mirror antisymmetric and reaches its largest magnitude near $|z| = 2.78$ m.

A signed amplification ratio was also calculated from the full-material and nonmagnetic OPERA results. In most of the screening chain, the iron increases the magnitude of the existing force. Near a zero crossing at approximately $|z| = 2.16$ m, however, the force changes sign between the two cases, with the resulting negative ratio at that location representing a force reversal. The additive material correction shown in Fig. 13 is therefore the more robust measure of the material contribution near force zero crossings.

Comparison of the independent analytical reconstruction with the $\mu_r = 1$ OPERA model produced

$$F_z^{\text{analytical}} = 0.996751\, F_z^{\text{OPERA},\mu_r=1} + 6.269 \times 10^{-8}\ \text{N},$$

with $R = 0.99993976$. The nearly unit slope, negligible intercept, and near-perfect correlation demonstrate that the independently integrated $J_\phi B_r$ force accurately reproduces the OPERA conductor-force solution when both calculations contain the same coil-only magnetic sources. The corresponding parity comparison is shown in Fig. 14.

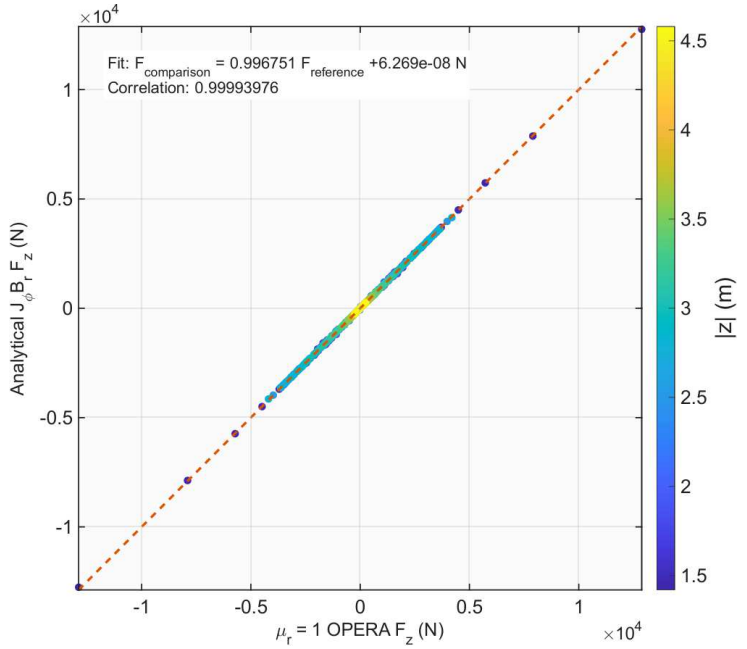


Figure 14: Parity comparison between the independent $J_\phi B_r$ force reconstruction and the OPERA model with the yoke and calorimeter assigned $\mu_r = 1$. The nearly unit slope and correlation coefficient close to one provide the direct validation of the analytical conductor-force calculation.

The agreement with the nonmagnetic solution establishes that the earlier difference between the analytical and full-material OPERA forces was primarily caused by flux redistribution by the nonlinear iron structures.

A conductor-specific material correction was defined as

$$\Delta F_{z,i}^{\text{material}} = F_{z,i}^{\text{OPERA,full}} - F_{z,i}^{\text{OPERA},\mu_r=1}. \tag{81}$$

This measured correction was then added to the independent coil-only result:

$$F_{z,i}^{\text{analytical,corr}} = F_{z,i}^{\text{analytical}} + \Delta F_{z,i}^{\text{material}}. \tag{82}$$

The corrected force profile closely overlaps the full-material OPERA result over the complete screening chain, as shown in Fig. 15.

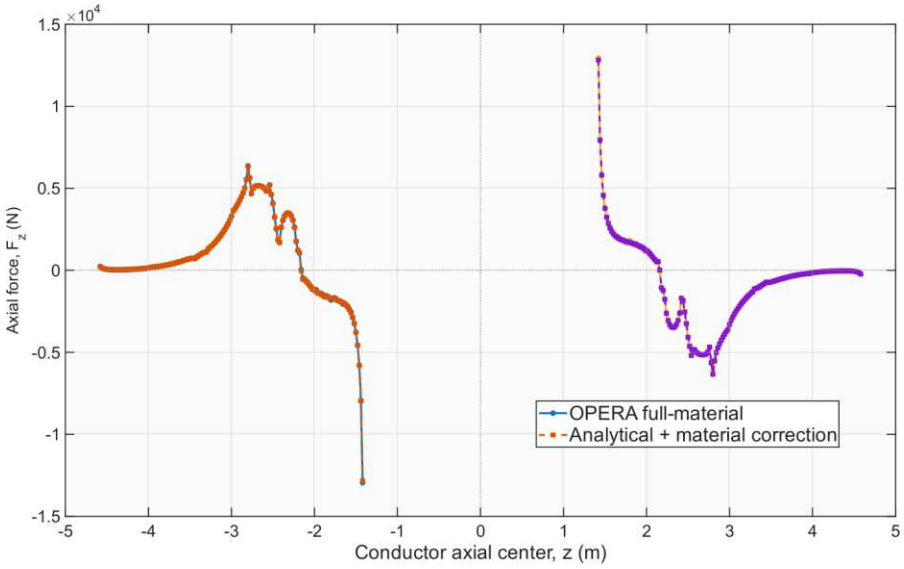


Figure 15: Full-material OPERA axial forces and the material-corrected analytical reconstruction. The conductor-specific correction recovers the dominant detector-facing load, the intermediate force reversals, the secondary concentration near $|z| = 2.8$ m, and the outer decay of the screening forces.

The corrected parity fit is

$$F_z^{\text{analytical,corr}} = 0.997591\, F_z^{\text{OPERA,full}} + 6.274 \times 10^{-8}\ \text{N},$$

with $R = 0.99996082$.

The corresponding corrected parity comparison is shown in Fig. 16.

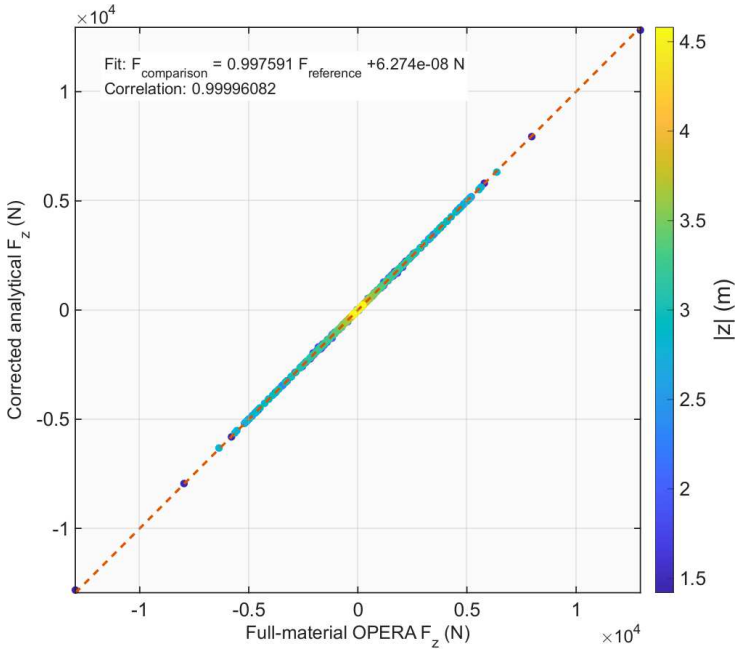


Figure 16: Parity comparison between the material-corrected analytical force and the full-material OPERA force. The remaining deviation is governed by the small difference between the analytical coil-only calculation and the $\mu_r = 1$OPERA solution.

The corrected residual satisfies

$$F_{z,i}^{\text{analytical,corr}} - F_{z,i}^{\text{OPERA,full}} = F_{z,i}^{\text{analytical}} - F_{z,i}^{\text{OPERA},\mu_r=1}.$$

The three force comparisons are summarized in Table 6.

Table 6: Linear parity fits for the optimized-model force comparisons. Each fit is F_comparison = a F_reference + b.

Comparison	Slope a	Intercept b (N)	Correlation R
Analytical vs. full-material OPERA	0.784182	4.932×10^{-8}	0.98091642
Analytical vs. $\mu_r = 1$ OPERA	0.996751	6.269×10^{-8}	0.99993976
Material-corrected analytical vs. full-material OPERA	0.997591	6.274×10^{-8}	0.99996082

The optimized-model force study establishes four principal results. First, the screening system carries large, spatially nonuniform internal axial loads despite the nearly zero net force of the complete symmetric magnet. Second, the largest individual load occurs in the detector-facing screening pair at $|z| = 1.42$ m, while a second major load concentration appears near $|z| = 2.8$ m. Third, the independent $J_\phi B_r$ reconstruction agrees closely with the nonmagnetic OPERA solution, with a fitted slope within approximately 0.33% of unity. Finally, the nonlinear yoke and calorimeter increase the cumulative absolute screening load by approximately 27.43 %, with the largest local material contribution occurring near $|z| = 2.78$ m. Adding the conductor-specific material contributions to the analytical coil-only forces recovers the complete full-material OPERA solution with close agreement. This decomposition therefore makes it possible to quantify and tabulate, for each individual conductor, the change in electromagnetic loading introduced by the nonlinear yoke and calorimeter. These results provide a conductor-resolved description of both the coil-generated forces and the additional loading introduced by the ferromagnetic detector components.

5 Conclusions

This work addressed the coupled problem of preserving a strong central detector field, suppressing the extended fringe field of a finite solenoid, and determining whether the resulting screening system introduces mechanically significant electromagnetic loads. A computational workflow was developed that combines analytical finite-thickness solenoid fields, Differential Evolution for nonlinear screening-coil geometry, and bounded weighted linear least squares for the segment current densities. The optimized configuration was then transferred to OPERA-3D for independent finite-element validation and conductor-level force analysis. A reduced two-solenoid benchmark was

used first to validate the OPERA force-extraction procedure against both a closed-form reduced-order model and a finite-thickness numerical calculation.

The optimized design consists of two mirror-symmetric screening chains with 24 primary segments per side. It preserves the approximately 3 T central field, producing a fitted peak of 2.99938 T, while strongly reducing the main-solenoid fringe field throughout the assessed external region. The remaining field error is concentrated primarily near the prescribed hard cutoff, where a continuous physical field must approximate an idealized discontinuity. The optimized geometry naturally assigns shorter segments and larger current densities near this transition, followed by progressively longer and more weakly excited segments in the smoother far-wing region. The corresponding OPERA model reproduced the optimized field behavior, confirming that the inverse-designed configuration can be represented consistently in a full three-dimensional magnetostatic calculation.

The full-model force study showed that global equilibrium does not imply small internal loading. The largest individual screening-conductor force was approximately 12.95 kN and occurred in the detector-facing mirror pair at $|z| = 1.42$ m, while a second broad load concentration appeared near $|z| = 2.8$ m. Although the net axial force of the complete symmetric system was effectively zero, the cumulative absolute screening load exceeded 600 kN. The independent $J_\phi B_r$ reconstruction agreed closely with the matched $\mu_r = 1$ OPERA model, validating the coil-only force calculation. The difference between the full-material and nonmagnetic OPERA solutions could therefore be used to quantify the conductor-specific loading introduced by the yoke and calorimeter. These nonlinear materials increased the cumulative absolute screening load by approximately 27.43 %, with the largest local material contribution occurring near $|z| = 2.78$ m. Adding these conductor-specific material contributions to the analytical coil-only forces reconstructed the complete full-material OPERA result with close agreement.

The next stage of the work should translate these electromagnetic forces into mechanical design requirements. This will require coupling the magnetostatic solution to a structural model containing realistic winding, insulation, and support properties; evaluating axial stress, radial loading, hoop stress, displacement, and deformation; and determining the support structure required to transmit the large opposing internal forces. The design should also be extended beyond on-axis field quality to include off-axis uniformity, superconducting operating margin, stored energy, quench protection, cryogenic performance, and manufacturable conductor and cable specifications. Additional mesh-sensitivity, current-scaling, and coupled electromagnetic–structural optimization studies would then establish whether the screening configuration can satisfy its field-suppression objective while remaining mechanically and technologically feasible.

Acknowledgments

This material is based upon work supported by the U.S. Department of Energy, Office of Science, Office of Workforce Development for Teachers and Scientists, Office of Science Graduate Student Research (SCGSR) program. The SCGSR program is administered by the Oak Ridge Institute for Science and Education for the DOE under contract number DE-AC05-06OR23100.

I would like to thank the Brookhaven National Laboratory Magnet Division and Vikas Teotia for providing the opportunity, resources, and technical environment to conduct this work. I am especially grateful to my mentors and collaborators at BNL for their guidance in superconducting magnet design, finite-element modeling, and electromagnetic force analysis. This work was conducted as part of the Ernest Courant Traineeship in Accelerator Science & Engineering Award No. DE-SC0020375 and benefited from the computational and research resources available at Brookhaven National Laboratory. **No export control**.

References

[1] Abada, A., M. Abbrescia, S. S. AbdusSalam, et al. 2019. “FCC-Ee: The Lepton Collider: Future Circular Collider Conceptual Design Report Volume 2.” *European Physical Journal Special Topics* 228 (2): 261–623. https://doi.org/10.1140/epjst/e2019-900045-4.

[2] Benedikt, M., K. Oide, F. Zimmermann, et al. 2015. *Status and Challenges for FCC-Ee*. https://arxiv.org/abs/1508.03363.

[3] Hervé, A. 2000. “Detector Magnets.” *IEEE Transactions on Applied Superconductivity* 10 (1): 389–94. https://doi.org/10.1109/77.828295.

[4] Yamamoto, Akira. 2009. “Detector Magnets.” *Reviews of Accelerator Science and Technology* 2: 27–44. https://doi.org/10.1142/S1793626809000205.

[5] Boscolo, M., F. Palla, G. Ammirabile, K. André, et al. 2025. “Status of the FCC-Ee Interaction Region Design.” *EPJ Techniques and Instrumentation*, ahead of print. https://doi.org/10.1140/epjti/s40485-025-00117-3.

[6] Callaghan, E. E., and S. H. Maslen. 1960. *The Magnetic Field of a Finite Solenoid*. NASA Technical Note D-465. National Aeronautics; Space Administration. https://ntrs.nasa.gov/citations/19980227402.
[7] Montgomery, D. Bruce. 1969. *Solenoid Magnet Design: The Magnetic and Mechanical Aspects of Resistive and Superconducting Systems*. Wiley-Interscience.
[8] Boscolo, M., A. Ciarma, H. Burkhardt, et al. 2025. "Non-Local Solenoid Compensation Scheme at the Future e^+e^- Circular Collider." *Nuclear Instruments and Methods in Physics Research Section A*. https://www.sciencedirect.com/science/article/pii/S0168900225009374.
[9] Jackson, John David. 1999. *Classical Electrodynamics*. 3rd ed. John Wiley & Sons.
[10] Grover, Frederick W. 1946. *Inductance Calculations: Working Formulas and Tables*. D. Van Nostrand Company.
[11] Storn, Rainer, and Kenneth Price. 1997. "Differential Evolution—a Simple and Efficient Heuristic for Global Optimization over Continuous Spaces." *Journal of Global Optimization* 11 (4): 341–59. https://doi.org/10.1023/A:1008202821328.
[12] Das, Swagatam, and Ponnuthurai N. Suganthan. 2011. "Differential Evolution: A Survey of the State-of-the-Art." *IEEE Transactions on Evolutionary Computation* 15 (1): 4–31. https://doi.org/10.1109/TEVC.2010.2059031.
[13] CEPC Study Group. 2018. *CEPC Conceptual Design Report: Volume 1 – Accelerator*. https://arxiv.org/abs/1809.00285.
[14] CEPC Accelerator Study Group. 2022. *Snowmass2021 White Paper: Circular Electron Positron Collider (CEPC)*. https://arxiv.org/abs/2203.09451.
[15] Sigmund, Ole, and Kurt Maute. 2013. "Topology Optimization Approaches: A Comparative Review." *Structural and Multidisciplinary Optimization* 48 (6): 1031–55. https://doi.org/10.1007/s00158-013-0978-6.

A Production Optimization Parameters

This appendix collects the physical inputs, geometric constraints, computational settings, objective-function coefficients, and adaptive-refinement criteria used for the production fixed-main-solenoid calculation. Parameters associated only with smoke tests, variable-radius comparison studies, disabled coverage penalties, and post-optimization cell diagnostics are omitted because they do not influence the optimized segment-level solution.

The objective-function coefficients should be interpreted as relative weights within the composite optimization objective. Their numerical magnitudes depend on the units and normalization of the field-error quantities they multiply and should therefore not be interpreted independently.

Table A1: Complete physical, geometric, numerical, and optimization parameters used for the production fixed-main-solenoid screening calculation.

Parameter	Configuration symbol	Value
Target magnetic field		
Vacuum permeability	mu0	$4\pi\times 10^{-7}$ H m^{-1}
Target peak field	B0	3.0 T
Target-field center	z0_mm	0 mm
Gaussian width	sigma_main_mm	1800 mm
Preserved target half-width	HALF_WIDTH_MM	1250 mm
Main-field tail tolerance	MAIN_TAIL_TOL_T	1.0×10^{-3} T
Screen-chain start offset	SCREEN_START_BEFORE_CLIFF_FRAC	0.08
Wing-region padding	WING_REACH_PAD_MM	150 mm
Minimum wing-region reach	WING_REACH_MIN_MM	600 mm
Coverage tolerance	COVERAGE_TOL_MM	60 mm
Cliff guard fraction	CLIFF_GUARD_FRAC	0.04
Fixed main solenoid		
Production operating mode	RUN_MODE	fixed_main
Main-solenoid inner radius	FIXED_MAIN_A1_M	2.00 m
Main-solenoid radial build	FIXED_MAIN_T_M	0.35 m
Main-solenoid outer radius	R_main,out	2.35 m
Main-solenoid axial length	FIXED_MAIN_L_M	2.60 m
Main-solenoid axial center	FIXED_MAIN_Z0_M	0 m
Main current-density mode	FIXED_MAIN_J_MODE	scale_to_B0
Main overshoot factor	MAIN_OVERSHOOT_FACTOR	1.0
Main-length mode	MAIN_LEN_MODE	coverage
Coverage peak mode	COVERAGE_PEAK_MODE	full
Screening-chain geometry and current bounds		

Parameter	Configuration symbol	Value
Maximum primary segments per side	SCREEN_PRIMARY_MAX_SEGMENTS	24
Maximum total segments per side	SCREEN_MAX_SEGMENTS	30
Adaptive segment-count increment	SCREEN_K_STEP	1
Minimum normalized chain start	SCREEN_Z_START_MIN_FRAC	0.90
Maximum normalized chain start	SCREEN_Z_START_MAX_FRAC	1.00
Minimum segment length	SEG_LEN_MIN_M	0.06 m
Maximum segment length	SEG_LEN_MAX_M	0.18 m
Minimum screening-current magnitude	SCREEN_J_MIN_A_PER_M2	1.0×10^{4} A m^{-2}
Maximum screening-current magnitude	SCREEN_J_MAX_A_PER_M2	1.8×10^{9} A m^{-2}
Minimum radial clearance	RADIAL_CLEARANCE_M	0.05 m
Minimum axial clearance	AXIAL_CLEARANCE_M	0.10 m
Chain-end safety margin	SCREEN_CHAIN_END_SAFETY_M	0.003 m
Geometry tolerance	GEOM_TOL_M	1.0×10^{-8} m
Signed trim-segment stage		
Enable signed trim segments	ALLOW_TRIM_SEGMENTS	True
Maximum trim segments per side	TRIM_MAX_SEGMENTS	6
Maximum trim-current magnitude	TRIM_J_MAX_A_PER_M2	2.5×10^{8} A m^{-2}
Trim DE iteration limit	TRIM_DE_MAXITER	200
Trim DE population factor	TRIM_DE_POPSIZE	18
Computational and reporting domain		
Computational axial domain	z_min_mm, z_max_mm	±10000 mm
Number of axial grid points	n_z	3201
Assessed half-domain	Z_REPORT_MM	8000 mm
Buffer taper floor	BUFFER_TAPER_FLOOR	0.04
Plotting half-domain	PLOT_X_MM	12000 mm
Winding assumptions		
Assumed main winding current per turn	I_TURN_MAIN_A	5000 A
Assumed screen current per turn	I_TURN_SCREEN_A	5000 A
Main winding packing fraction	LAMBDA_PACK_MAIN	0.70
Screen winding packing fraction	LAMBDA_PACK_SCREEN	0.70
Cancellation-region definitions and current-solve weights		
Cancellation-region tolerance	CANCEL_TOL_T	1.0×10^{-3} T
Cancellation-region weight	W_CANCEL	1.0×10^{8}
Early-cancellation start fraction	EARLY_CANCEL_START_FRAC	0.88
Outer-edge fractional extent	EDGE_OUTER_FRAC	0.35
Early-cancellation weight	W_EARLY_CANCEL	8.0×10^{7}
Outer-edge weight	W_EDGE_OUTER	3.0×10^{8}
Far-wing weight	W_FAR_WING	1.2×10^{8}
Peak and central-field objective penalties		
Peak-height penalty	PEAK_HEIGHT_WEIGHT	8.0×10^{13}
Center-point penalty	CENTER_POINT_WEIGHT	1.5×10^{14}
Near-peak RMSE penalty	PEAK_REGION_RMSE_WEIGHT	4.0×10^{11}
Center RMSE penalty	CENTER_RMSE_WEIGHT	1.5×10^{11}
Shoulder RMSE penalty	SHOULDER_RMSE_WEIGHT	8.0×10^{9}
Cancellation-region RMS penalty	CANCEL_RMS_WEIGHT	1.5×10^{10}
Cancellation-region maximum penalty	CANCEL_MAX_WEIGHT	4.0×10^{9}
Negative-center penalty	NEGATIVE_CENTER_WEIGHT	1.0×10^{14}
Peak-curvature penalty	PEAK_CURVATURE_WEIGHT	6.0×10^{11}
Peak-slope penalty	PEAK_SLOPE_WEIGHT	2.0×10^{11}
Wing, edge, and sign-asymmetric penalties		
Early-cancellation RMSE penalty	EARLY_CANCEL_RMSE_WEIGHT	1.5×10^{10}
Outer-edge RMSE penalty	EDGE_OUTER_RMSE_WEIGHT	1.5×10^{11}
Outer-edge maximum penalty	EDGE_OUTER_MAX_WEIGHT	6.0×10^{10}
Far-wing RMSE penalty	FAR_WING_RMSE_WEIGHT	9.0×10^{10}
Far-wing maximum penalty	FAR_WING_MAX_WEIGHT	4.0×10^{10}
Wing-oscillation penalty	OSCILLATION_WEIGHT	1.5×10^{11}
Positive exterior-field penalty	POSITIVE_OUTSIDE_WEIGHT	5.0×10^{11}
Negative-undershoot penalty	NEGATIVE_UNDERSHOOT_WEIGHT	6.0×10^{10}
Realizability penalties		
Segment-count penalty	SEGMENT_COUNT_WEIGHT	5.0×10^{10}

Parameter	Configuration symbol	Value
Minimum turns per segment	MIN_TURNS_PER_SEGMENT	3
Low-turn penalty	LOW_TURN_PENALTY_WEIGHT	2.0×10^{10}
Current-roughness penalty	CURRENT_ROUGHNESS_WEIGHT	4.0×10^{10}
Length-irregularity penalty	LENGTH_IRREGULARITY_WEIGHT	3.0×10^{10}
Thresholds and stall criteria		
Maximum outer-field threshold	MAX_OUTER_PEAK_GOOD_ENOUGH_T	1.2×10^{-2} T
Outer-edge RMSE threshold	EDGE_OUTER_RMSE_GOOD_ENOUGH_T	5.0×10^{-3} T
Far-wing RMSE threshold	FAR_WING_RMSE_GOOD_ENOUGH_T	2.0×10^{-3} T
Far-wing maximum threshold	FAR_WING_MAX_GOOD_ENOUGH_T	6.0×10^{-3} T
Relative peak-shape threshold	PEAK_SHAPE_GOOD_ENOUGH_REL	8.0×10^{-2}
Minimum strict relative improvement	STRICT_MIN_REL_IMPROVE	3.0×10^{-3}
Strict stall patience	STRICT_STALL_PATIENCE	3
Minimum broad relative improvement	SCREEN_MIN_REL_IMPROVE	1.0×10^{-3}
Broad RMSE stopping threshold	SCREEN_RMSE_GOOD_ENOUGH_T	2.5×10^{-4} T
Adaptive split and candidate-selection weights		
Split outer-edge emphasis	SPLIT_EDGE_OUTER_EMPHASIS	4.0
Split far-wing emphasis	SPLIT_FAR_WING_EMPHASIS	2.5
Split early-cancellation emphasis	SPLIT_EARLY_CANCEL_EMPHASIS	1.5
Split oscillation weight	SPLIT_OSC_WEIGHT	2.0
Selection outer-edge weight	SEL_EDGE_OUTER_W	4.0
Selection far-wing weight	SEL_FAR_WING_W	3.0
Selection outer-peak weight	SEL_OUTER_PEAK_W	2.0
Selection cancellation weight	SEL_CANCEL_W	1.0
Selection peak-shape weight	SEL_PEAK_SHAPE_W	8.0×10^{-2}
Differential-Evolution and local-search budgets		
Random-number seed	RNG_SEED	11
Parallel worker setting	MAX_WORKERS	-1
Screen DE iteration limit	SCREEN_DE_MAXITER	350
Screen DE population factor	SCREEN_DE_POPSIZE	24
Initial screen capacity	SCREEN_K_INIT	2
Structure DE iteration limit	STRUCT_DE_MAXITER	240
Structure DE population factor	STRUCT_DE_POPSIZE	12
Independent DE restarts	DE_RESTARTS	2
Local-polish iteration limit	LOCAL_MAXITER	4000

The post-optimization cell-level analysis uses separate discretization and diagnostic settings. Because those quantities are evaluated only after the segment-level field optimization has converged, they are not included in Table A1.

B Final Optimized Fit Metrics

Table B1 summarizes the principal field-quality, coverage, and current-distribution metrics obtained for the final production solution. The reported configuration contains 24 primary screening segments per side and no accepted signed trim segments. The complete machine-readable output is retained in the corresponding CSV file.

Table B1: Principal field-quality and screening-system metrics for the final fixed-main-solenoid optimization. The central field is reproduced accurately, although some strict acceptance criteria are not satisfied.

Quantity	Symbol	Value
Optimized segmentation		
Segments per side	N_seg	24
Primary segments per side	N_primary	24
Accepted trim segments per side	N_trim	0
Central-field reconstruction		
Target peak field	B_0	3.0000 T
Optimized peak field	B_peak^fit	2.99938 T
Peak-field error	Δ B_peak	-6.21×10^{-4} T
Relative peak error	Δ B_peak/B_0	-0.0207%
Near-peak RMSE	RMSE_peak	4.05×10^{-3} T
Center-plus-wing RMSE	RMSE_center+wing	2.49×10^{-2} T
Full-domain RMSE	RMSE_total	6.73×10^{-2} T
Fringe-field performance		

Quantity	Symbol	Value
Physical-wing RMS field	B_wing,RMS	1.35×10^{-2} T
Maximum physical-wing field	max |B_wing|	6.09×10^{-2} T
Edge-outer RMS residual	RMSE_edge	1.74×10^{-2} T
Far-wing RMS residual	RMSE_far	9.34×10^{-3} T
Maximum far-wing residual	max |Δ B_far|	2.35×10^{-2} T
Field at the assessed-domain edge	|B_z(z_report)|	3.55×10^{-3} T
Screen-chain coverage		
Screen-chain start	z_screen^start	1250.0 mm
Screen-chain end	z_screen^end	9800.0 mm
Uncovered cancellation length	L_uncovered	0 mm
Optimized screening currents		
Minimum current-density magnitude	min |J_screen|	3.45×10^{6} A m^{-2}
Maximum current-density magnitude	max |J_screen|	1.96×10^{8} A m^{-2}
Exponential decay coefficient	k	2.892
Exponential-fit coefficient of determination	R^2	0.9857
Strict field-quality thresholds satisfied	---	No

The optimized screening system preserves the central detector field to better than 0.03%. The remaining error is dominated by the discontinuous target transition and by low-amplitude oscillatory structure in the external cancellation region. Because the screening chains cover the complete required axial interval, the remaining wing residual cannot be attributed to a geometric coverage gap. Instead, it reflects the finite segmentation and the imposed geometric, realizability, and current-density constraints.

C Optimized Solenoid and Screening-Chain Parameters

The final winding configuration is summarized in Tables C1 and C2. Because the optimized geometry is mirror symmetric, only the right screening chain is tabulated. The left-side segment corresponding to right-side segment i is obtained through

$$z_{0,i}^{\mathrm{left}} = -z_{0,i}^{\mathrm{right}}, \tag{83}$$

with the same length, radial dimensions, current-density magnitude, ampere-turns, and estimated turn count. The screening-current direction is opposite to that of the main solenoid.

Table C1: Fixed main-solenoid parameters used in the production optimization. Ampere-turns and turn count assume a 5000 A conductor current.

Quantity	Value
Axial center, z_0	0 mm
Axial length, L	2600 mm
Inner radius, a_1	2000 mm
Outer radius, a_2	2350 mm
Current density, J	1.3282×10^{7} A m^{-2}
Integrated ampere-turns, NI	8.4608×10^{6} A turn
Estimated turn count	1693

Table C2: Optimized parameters for the right screening chain. Segments 1–24 lie between the detector-facing region and far wing; the left chain is obtained by reflection.

Seg.	z_0 (mm)	L (mm)	J (A m^{-2})	NI (A turn)	Turns
1	1287.9	75.8	-1.960×10^{8}	1.040×10^{5}	21
2	1396.6	141.5	-1.734×10^{8}	1.718×10^{5}	35
3	1551.7	168.6	-1.587×10^{8}	1.873×10^{5}	38
4	1726.1	180.2	-1.442×10^{8}	1.819×10^{5}	37
5	1905.5	178.7	-1.299×10^{8}	1.625×10^{5}	33
6	2084.4	179.2	-1.165×10^{8}	1.462×10^{5}	30
7	2262.2	176.4	-1.041×10^{8}	1.286×10^{5}	26
8	2438.3	175.8	-9.294×10^{7}	1.143×10^{5}	23
9	2617.1	181.9	-8.267×10^{7}	1.053×10^{5}	22
10	2806.8	197.4	-7.294×10^{7}	1.008×10^{5}	21
11	3016.2	221.4	-6.352×10^{7}	9.842×10^{4}	20
12	3251.7	249.7	-5.441×10^{7}	9.511×10^{4}	20
13	3514.6	276.2	-4.593×10^{7}	8.879×10^{4}	18

Seg.	z_0 (mm)	L (mm)	J (A m^{-2})	NI (A turn)	Turns
14	3807.3	309.1	-3.822×10^7	8.269×10^4	17
15	4138.3	352.9	-3.147×10^7	7.775×10^4	16
16	4519.1	408.8	-2.511×10^7	7.185×10^4	15
17	4954.1	461.3	-1.981×10^7	6.397×10^4	13
18	5436.4	503.2	-1.547×10^7	5.449×10^4	11
19	5963.0	550.0	-1.203×10^7	4.631×10^4	10
20	6540.2	604.4	-9.313×10^6	3.940×10^4	8
21	7174.1	663.5	-7.178×10^6	3.334×10^4	7
22	7866.4	721.1	-5.542×10^6	2.797×10^4	6
23	8609.7	765.5	-4.329×10^6	2.320×10^4	5
24	9396.2	807.5	-3.453×10^6	1.952×10^4	4

The optimized chain exhibits a systematic redistribution of current and conductor length with axial position. The detector-facing segments are short and carry the largest current-density magnitudes, providing the local control needed near the abrupt target cutoff. Farther from the detector, the optimized segments become progressively longer while their current-density magnitudes and ampere-turns decrease. This trend reflects the transition from localized correction of the hard-edge region to broad suppression of the slowly varying far-field tail.

Supplementary Files

This is a list of supplementary files associated with this preprint. Click to download.

- Table1.png
- Table2.png
- Table3.png
- Table4.png
- Table5.png
- Table6.png
- TableA1.png
- TableB1.png
- TableC1.png
- TableC2.png